Static and dynamic testing and modelling of aluminium joints with flow-drill screw connections

Johan Kolstø Sønstabø[a,b], David Morin[a,b,*], Magnus Langseth[a,b]

[a]*Centre for Advanced Structural Analysis (CASA), Norwegian University of Science and Technology (NTNU), NO-7491 Trondheim, Norway*
[b]*Structural Impact Laboratory (SIMLab), Department of Structural Engineering, NTNU, NO-7491 Trondheim, Norway*

Abstract

A new component test suited for quasi-static and dynamic testing of flow-drill screw connections is presented. The component specimen was made of two different aluminium alloys, and included connections with two material combinations. Large-scale finite element simulations were carried out of each test, in which the connections were modelled with a constraint-based macroscopic model. An improvement of the connection modelling technique is presented. The model was calibrated to cross tension, cross mixed and single lap-joint tests, and validated with peeling and the component tests.

Keywords: Flow-drill screw, Dynamic testing, Connection, Macroscopic, Component

1. Introduction

An increasing number of different aluminium alloys is used in the production of cars, to meet requirements of vehicle weight reduction. This gives rise to challenges in the joining of parts, because traditional techniques such as for instance spot welding becomes problematic. Among other techniques, flow-drill screws (FDS) are therefore commonly used to join dissimilar materials in the load-carrying structure of cars. This joining technique combines flow drilling and thread forming in a single procedure, where the screw is both functioning as tool and as fastener, which makes the process suited for automation. An advantage with this technique is that it requires tool access to one side only, as opposed to spot welding or self-piercing riveting, for instance, where access to both sides is required. More than two plates may be joined, and the process can be used with and without a pre-hole in the top plate.

Connections such as FDS play an important role for the structural integrity and energy dissipation during car crashes, and knowledge of their mechanical behaviour under crash loadings is therefore of importance to designers in order to make safe cars. Thus, they rely on experimental testing, which typically involve loading specimens consisting of plates joined with one or more screws until failure. Different levels of complexity are

---

achieved by varying the specimen design and loading conditions, ranging from simple tests with two plates and one screw (single-connector tests) to component tests with several screws and complex loadings.

There exist several studies with single-connector testing of FDS connections. Szlosarek et al. (2013) presented a new testing and analysis method, and used it for FDS connections between a carbon fibre reinforced polymer and aluminium. Skovron et al. (2014) presented an experimental study on a connection between sheets of aluminium alloy AA 5052-O. They studied how process parameters affect the geometry of the assembled connection, and performed mechanical tests of the connections to support the findings. Sønstabø et al. (2015) carried out an experimental programme to characterise an FDS connection between rolled sheets of AA 6016 in temper T4. The results were compared to equivalent tests on self-piercing rivet connections. Furthermore, Skovron et al. (2015) evaluated the effect of thermally assisting the FDS process by pre-heating the plates with an external heat source. They performed mechanical tests on connections between sheets of AA 6063 T5A. A study on an FDS connection between AA 6016 T4 and AA 6063 T6 was briefly presented by Sønstabø et al. (2016), who used the results to evaluate large-scale finite element modelling techniques for connections.

However, information regarding component tests with FDS connections is limited in the scientific literature. Sønstabø et al. (2015) carried out quasi-static and dynamic axial crushing tests of a single-hat crash box joined with FDS. A limitation with this test is that the global force-displacement behaviour was dominated by large material deformations outside of the connections (progressive buckling), which makes it difficult to evaluate the behaviour of the connections. A quasi-static T-component test was carried out by Sønstabø et al. (2016). In this test the material deformation outside of the connections was limited, and the loading on the connections was shear dominated. A limitation with this test is that it is difficult to transfer the test boundary conditions to numerical simulations, which makes it unsuitable for validation purposes.

Although limited information about component testing of FDS connections is available, several studies on component tests with other connection types exist. Some of them are referenced in the following. Porcaro et al. (2004) carried out quasi-static and dynamic axial crushing tests on double-hat sections made of aluminium sheets joined with self-piercing rivets. The results were used to evaluate the accuracy and robustness of a numerical model. Belingardi et al. (2005) performed similar crushing tests on four different steel sections joined by adhesive bonding, to assess the applicability of structural bonding in the crash-absorbing parts of the car structure. Xiang et al. (2006) carried out quasi-static axial crushing tests of a top-hat section consisting of steel sheets joined with spot welds. The results were used to validate a numerical model, which was utilised to optimise the design of the top-hat section with respect to crashworthiness. Zhou et al. (2011) executed axial crushing tests on an S-shaped frontal frame structure of a car body. The component was made of steel and aluminium sheets that were spot welded together. The aim of this study was to evaluate the influence of different design parameters on the crashworthiness of the structure. A three-point bending-like test was carried out by Chen (2001), using components consisting of different closed top-hat sections of aluminium sheets. The sections were joined using spot welding and filled with an aluminium foam core. Carlberger and Stigh (2010) performed similar bending

tests on an aluminium-steel component. The aim of this study was to evaluate how different joining techniques affect the impact properties of the structure. They tested with adhesive bonding, screws and nuts, and hybrid joints consisting of both. A similar set-up was used by Qi et al. (2016) to test a double-hat beam composed of an aluminium upper hat and a high strength steel lower hat, riveted together. Hoang et al. (2012) performed quasi-static T-component tests with two load configurations on a component consisting of two aluminium extrusions. They were joined using self-piercing rivets made of aluminium. The aim of the study was to assess the applicability of rivets made of aluminium under crash loadings.

Since limited information on the topic exists, a new component test for FDS connections is presented, where the dominating deformation mode is taking place in the connections, and at the same time has relevant and sufficiently complex loadings. A test where the failure of connections can be discerned in the global response of the specimens is desired. Moreover, except for the study of Sønstabø et al. (2015), no scientific publications have been found on dynamic testing of FDS connections. Thus, there is also a lack of knowledge about their dynamic behaviour. An aim of this paper is to remedy both.

In addition to experimental testing, car designers rely heavily upon large-scale finite element crash simulations. Due to time step requirements, connections such as FDS cannot be modelled in detail. Instead, macroscopic models are used, in which the connections are excluded, but their global behaviour is modelled as a constraint or with simple elements. Such models must be calibrated and validated with experimental tests, for which component tests are important to assess the models' ability to represent complex loadings (Sønstabø et al., 2016).

This paper presents an innovative component test suited for quasi-static and dynamic testing of FDS connections between aluminium extrusions, for validation of large-scale numerical simulations. The component specimen was made of two different aluminium alloys, and included connections with two material combinations. An improved modelling technique for large-scale finite element simulations was presented, and calibrated using cross tension, cross mixed and single lap-joint tests, and validated with peeling tests and the component tests. The component tests are presented first. Then follows a section about the finite element modelling. The component simulations are then presented and discussed, before a summary and conclusions. The single-connector tests are briefly presented in the appendix.

2. Component tests

In this section the component tests are presented. The component design is discussed first. The quasi-static test is then introduced, with a discussion of the test set-up, followed by the results. Thereafter follows the set-up of the dynamic component test and an analysis of the results.

2.1. Component design

For validation purposes, the following desirable properties were the basis for the design of the component

test specimen:

– Relevant and sufficiently complex loadings on the connections were desired. During a car crash, loadings

are highly complex and difficult to evaluate. The component tests should represent relatively controlled

deformation modes.

– The component specimen was designed such that material deformation outside the connections was limited.

A test where the dominating deformation mode takes place in the connections, and where the failure of

connections can be discerned in the global response of the specimens, was desired.

– Manageable boundary conditions was essential for test repeatability as well as for reproducibility in finite

element models.

The resulting component design is shown in Fig. 1a. It consisted of a vertical two-chamber extrusion profile

made of alloy AA 6005 T6 produced by SAPA, joined to two rectangular profiles of alloy AA 6060 T6 produced by

Hydal Aluminium Profiler. Angle sections cut out of the rectangular profile were used to join the parts. Thus, the

joint consisted of two different FDS connections, one between two faces of the 6060-extrusion and one between

the 6060 and the 6005-extrusion (hereafter denoted the *HH-connection* and *HS-connection*, respectively). In both

connections a case hardened carbon steel flow-drill screw from EJOT was used, and a pre-hole of 7 mm diameter

was drilled in the top plate. Schematic drawings of the two connections are shown in Figs. 1b and 1c, where

nominal dimensions of the screw are included. Nominal dimensions of the component specimen and screw

locations are given in Fig. 1d, and schematic drawings of the extrusion profiles are presented in Figs. 1e and 1f.

As seen in the figures, the specimen was simply supported. The supports were made of solid steel, round with a

diameter of 50 mm, and placed 600 mm apart. The specimens were joined by EJOT GmbH & Co. KG.

Engineering stress-strain curves of the extrusions were obtained with uniaxial tensile tests in the extrusion,

diagonal and transversal directions. Representative curves are presented in Fig. 2, and Lankford coefficients are

presented in Table 1. As seen, the 6005-alloy was strongest with approximately 50 % higher yield stress, while

the 6060-alloy was approximately 20 % more ductile. The alloys exhibit limited anisotropy with respect to the

flow stress, and significant anisotropy with respect to plastic flow. It has previously been shown that the 6005-

alloy exhibits some strain-rate sensitivity (Børvik et al., 2005), while the 6060-alloy is only slightly strain-rate

sensitive (Chen et al., 2009).

The component design and test set-ups were inspired by the work of Grimsmo et al. (2015), who conducted

quasi-static and dynamic tests on a double-sided beam-to-column joint configuration to study the behaviour of

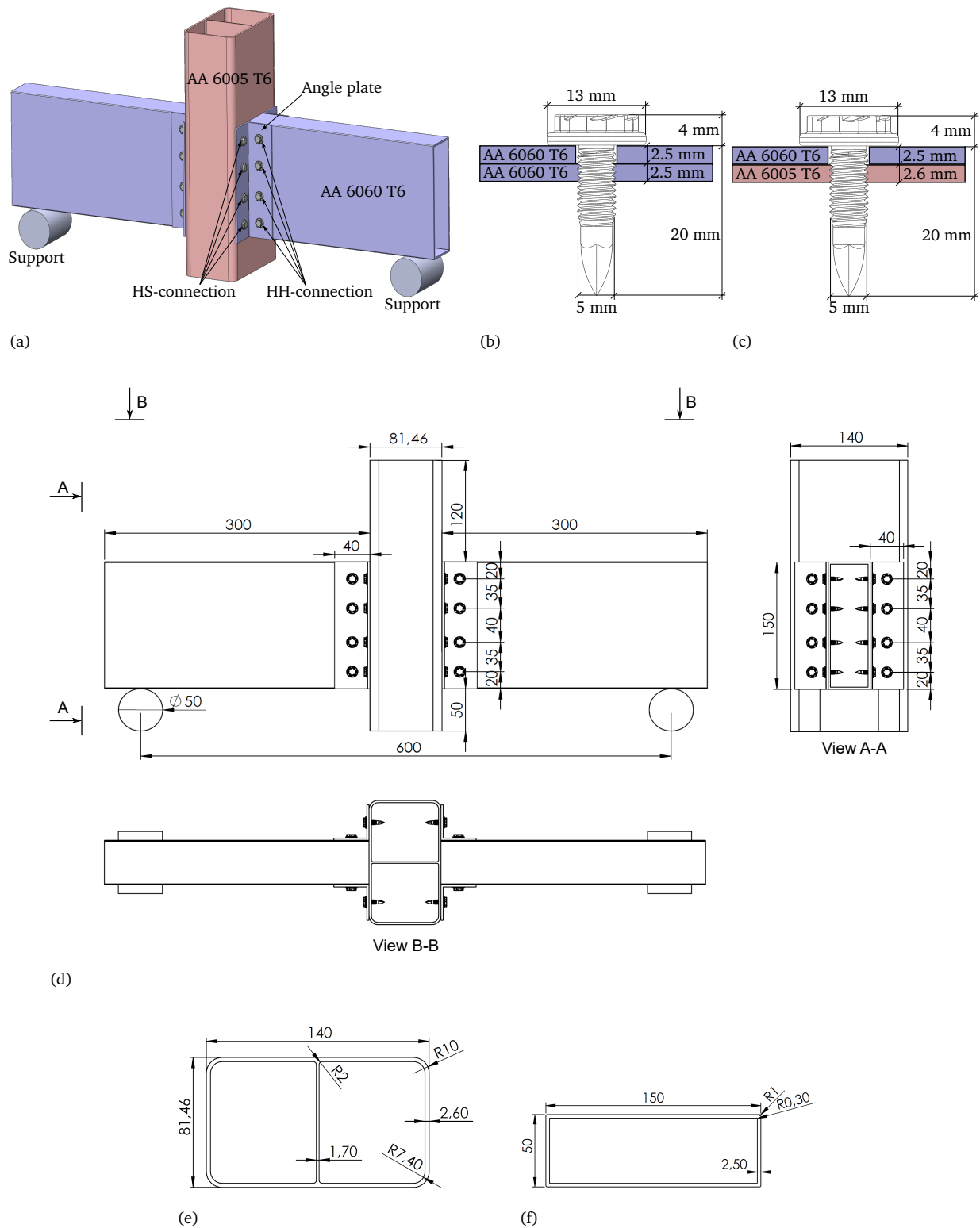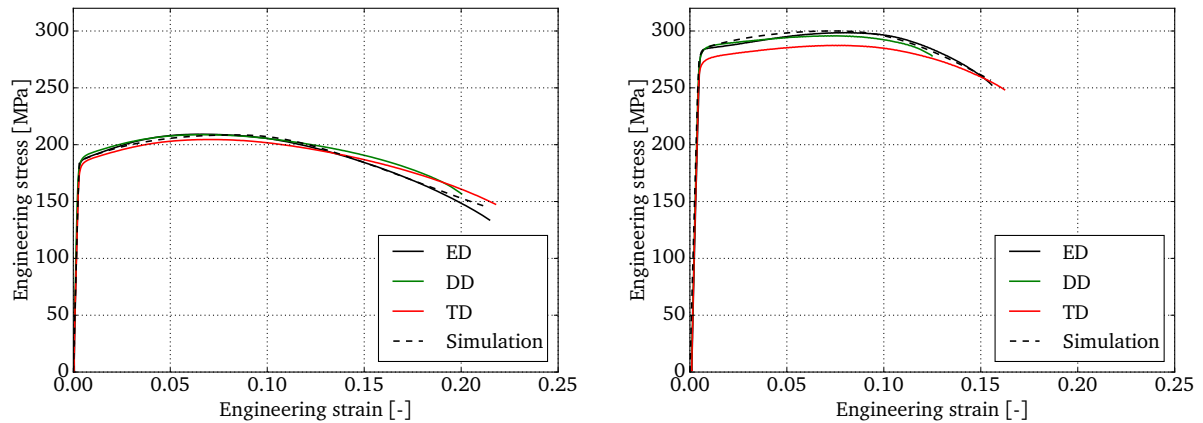structural joints subjected to impact loading.

Fig. 1. Component design. (a) CAD model of component. (b) HH-connection. (c) HS-connection. (d) Schematic drawing of component (front, end and top view) (e) The 6005 extrusion profile. (f) The 6060 extrusion profile. All dimensions are nominal values.

Fig. 2. Representative engineering stress-strain curves from uniaxial tensile tests in the extrusion (ED), diagonal (DD) and transversal (TD) directions of the (a) AA 6060 T6 and (b) AA 6005 T6 profiles. Curves from simulations of the tests are included.

Table 1

Lankford coefficients of the extrusion materials.

Material	R_{ED}	R_{DD}	R_{TD}
AA 6060 T6	0.58	0.25	2.26
AA 6005 T6	0.58	0.16	2.39

2.2. Quasi-static set-up

Fig. 3 depicts the quasi-static test set-up. The supports were firmly mounted to a regular tensile test machine. Care was taken to ensure that the supports and specimen were placed symmetrically about the centre of the test rig. The specimen was held in place with rubber straps. L-shaped steel bars were welded to the sides of each support, to hold the specimen in place in case of out-of-plane rotations. Such rotations did not occur in any of the tests, including the dynamic ones.

A downward-directed force was applied to the top of the vertical profile of the specimen, by pushing down a circular solid steel plate at a constant velocity of 10 mm/min. The force history was recorded with a load cell connected in series between the steel plate and the cross beam of the test machine. The vertical displacement of the steel plate and the deformation of the specimen were recorded with cameras taking one picture per second during the test. Five replicates were performed.

2.3. Quasi-static results

The resulting force-displacement curves are plotted in Fig. 4. As seen, excellent repeatability was obtained. The force increased gradually as the specimen was loaded until flattening out to a plateau at approximately 15 kN, caused by buckling of the inner wall in the vertical profile. After the plateau the force further increased until
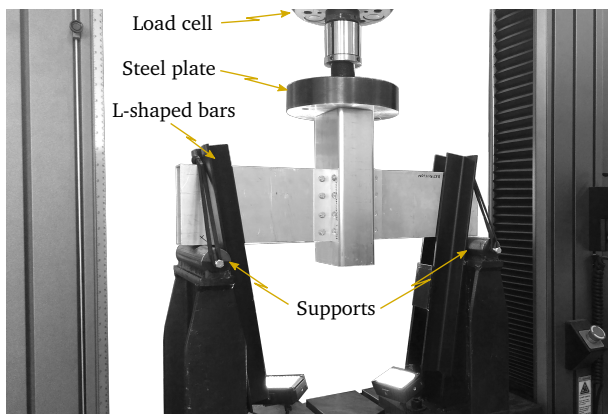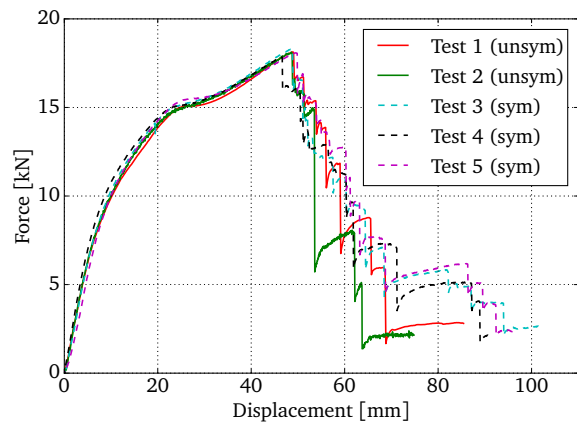
6

Fig. 3. Quasi-static test set-up.

Fig. 4. Force-displacement curves from quasi-static component tests.
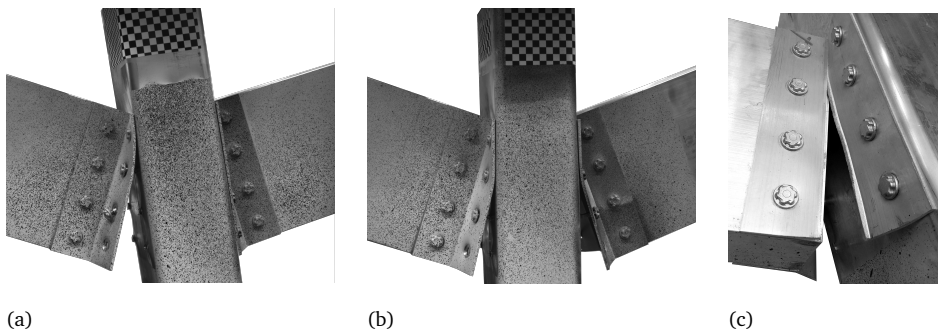

(a)

(b)

(c)

Fig. 5. Pictures of components during quasi-static testing showing (a) unsymmetrical and (b) symmetrical specimen deformation, and (c) material failure in test 4.

reaching the maximum capacity of the specimen at approximately 18 kN. Global failure then initiated by a rapid failure in one of the lowest HS-connections. Soon after, the corresponding connection on the other sides failed in the same manner. Failure of the lowest connections redistributed the load to the next screws, and so on, resulting in propagating connection failure along the rows of screws.

In the first two tests failure took place on one side of the vertical profile, resulting in an unsymmetrical specimen deformation mode. For the remaining three tests failure occurred symmetrically about the vertical profile. This is shown with pictures taken during testing in Figs. 5a and 5b. A possible cause for triggering different failure modes is variations in structural capacity and ductility of the connections. This could result in one side of the vertical profile being weaker than the other, possibly resulting in an unsymmetrical deformation mode.

In test 4, one of the four angle sections fractured in the corner, rather than failing in the connections. This is shown in Fig. 5c. In the three remaining angle sections connection failure occurred. The specimen deformed nevertheless symmetrically. Despite the fractured angle section, the force-displacement curve was similar to the other tests. Test 4 was left out from the plots in the remaining of the paper.

2.4. Dynamic set-up

The dynamic component tests were carried out with a pendulum accelerator, which is a device designed for impact testing of structural components, see Fig. 6a. Details on the rig and its functions have previously been reported by Hanssen et al. (2003), hence only the main aspects are explained herein. The specimen was mounted on the supports with rubber bands as in the quasi-static test, and the supports were fastened to a reaction wall, which weighs 150 000 kg and rests on neoprene supports. The specimen was impacted by a trolley with mass 399.9 kg travelling on rails, accelerated by a rotating arm. The arm was controlled by a hydraulic/pneumatic actuator. With this set-up the contact between the trolley and the arm ceases after a certain rotation, and the
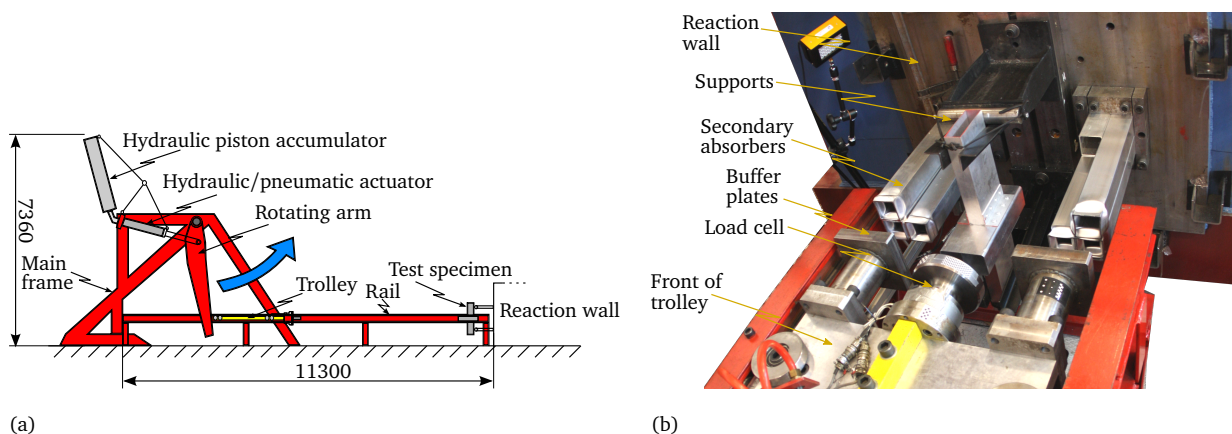

(a)

(b)

Fig. 6. Dynamic test set-up. (a) Illustration of the dynamic test rig (Grimsmo et al., 2015). (b) Picture showing details of the dynamic test set-up.

trolley subsequently travels down the rails at a near constant velocity. The velocity is controlled by varying the pressure in a hydraulic piston accumulator. More details of the test set-up are provided by Fig. 6b.

When the trolley impacts the specimen, the double-chamber profile is accelerated towards the reaction wall, leading to dynamic loading of the connections. After approximately 100 mm displacement after impact, buffer plates on the trolley hit a set of secondary crash absorbers. This is necessary since the specimen does not absorb enough energy to stop the trolley.

Four high-speed cameras were utilized to capture the test. Two were aimed towards the top of the specimen where the impact occurred, and the remaining two at the connections in one of the four angle sections. The cameras took pictures at rates ranging between 20 000 and 30 000 frames per second. The impact velocity was measured with a photocell system, mounted on top of one of the rails. A laser mounted on the floor measured the displacement of the reaction wall (it was verified that the reaction wall displacement was negligible).

A load cell was mounted between the trolley and the specimen. It consisted of two circular solid steel plates and a thin-walled steel cylinder. Two strain gauges were mounted on the cylinder. Assuming that the load cell behaved elastically, the force was calculated from the average strain from the gauges. Adequate accuracy of the load cell was verified beforehand. The sampling rate of the load cell and laser was 250 kHz.

The trolley displacement was calculated from the force signal, by dividing with the mass of the trolley (Newton's second law) and integrate the acceleration twice in time. The obtained displacement was verified with digital image correlation (DIC), using the pictures from the high-speed cameras (readers are referred to Fagerholt (2012) for details on DIC).

Five repetitions were carried out, all with an impact velocity of 7 m/s. In each test care was taken to place the specimen symmetrically on the supports.

2.5. Dynamic results

Fig. 7 shows the force-time curves measured by the load cell for all five repetitions. As seen, adequate test repeatability was achieved. Immediately after the first impact a peak force developed and then rapidly decreased and oscillated around zero for some time. Approximately 1 ms into the test the force somewhat increased again, still oscillating significantly. At 2 ms the oscillations stabilised noticeably, and the force steadily increased to a maximum between 15 and 20 kN, before decreasing again.

The oscillations in the force recordings were expected and is a result of the dynamic nature of the test. Throughout the test the specimen exerted many impulses on the front of the load cell. These impulses generated stress waves travelling through the load cell, into the trolley, and to the end of the trolley where they were reflected. As a consequence, throughout the test a myriad of stress waves travelled back and forth in the load cell, causing the strain signal (and thus the force signal) to oscillate.

From the high-speed camera recordings it was evident that after the initial impact the specimen gained a higher velocity than the trolley, and therefore departed from the trolley and the contact between the load cell and
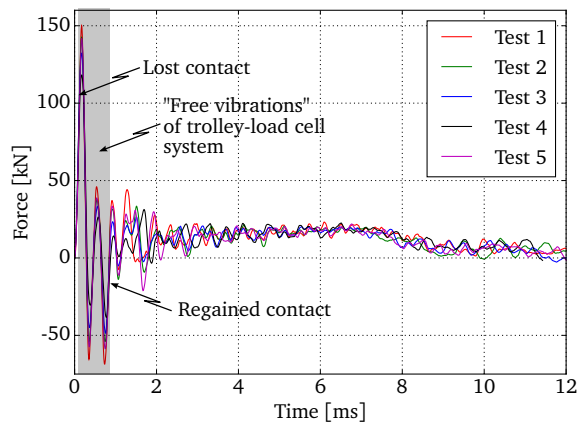
9

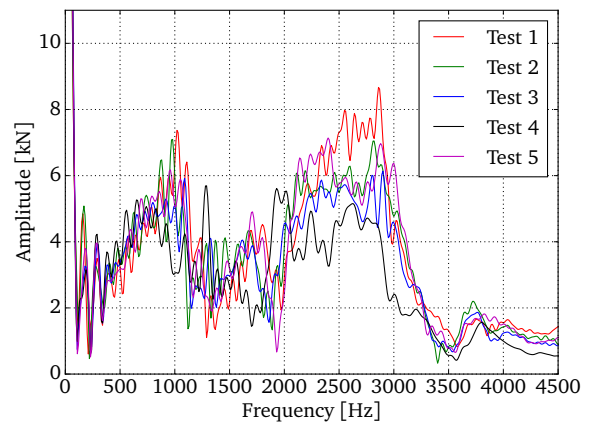**Fig. 7.** Force-time curves from dynamic component tests.

Fig. 8. Fast Fourier transform of the force signals.

specimen ceased. The time period without contact was measured to last approximately 0.8 ms, and is indicated with a shade of grey in Fig. 7. Within this time period the trolley-load cell system vibrated "freely", such that the force signal at this time only contained information from the trolley-load cell system. By measuring the period of the first oscillation following the initial peak, the frequency of the vibration may be calculated as approximately 2700 Hz. This is supported by Fig. 8, which shows the fast Fourier transform of the force signal from each test. It is seen that there were significant frequency components in the vicinity of 2700 Hz.

Hanssen et al. (2003) argued for filtering of the load cell signal. When examining Figs. 7 and 8 it may be tempting to filter out frequencies higher than, for instance, 2000 Hz with a low-pass filter. However, Fig. 9 disfavours such a decision. The figure shows a contour plot of a short time Fourier transform of the force signal from test 1. The force signal was divided into smaller segments, and for each segment the fast Fourier transform was computed and the frequency spectrum plotted. Thus Fig. 9 shows how the frequency spectrum of the force signal varied throughout the test. From the figure it is evident that during the time without contact between the load cell and the specimen the significant frequency components ranged approximately between 1500 and 4000 Hz. After 2 ms, when firm contact between the specimen and trolley was achieved, the significant frequency components ranged from 0 to approximately 2000 Hz. Thus, filtering out the frequencies higher than 2000 Hz would not reveal any new information, but lead to a degradation of the quality of the results. Therefore it was decided to not filter the results, except for some high-frequency noise in the force signals which were filtered out with a zero-phase Butterworth filter with a cut-off frequency of 20 000 Hz.

A representative curve of force versus trolley displacement is plotted in Fig. 10, along with a corresponding quasi-static force-displacement response. As seen, the two curves overlay each other, which indicates that no global inertia effects in the specimen influenced the impact. This is due to the fact that the impacting mass was large compared to the mass of the specimen. The results did not suggest any significant rate effects on the global
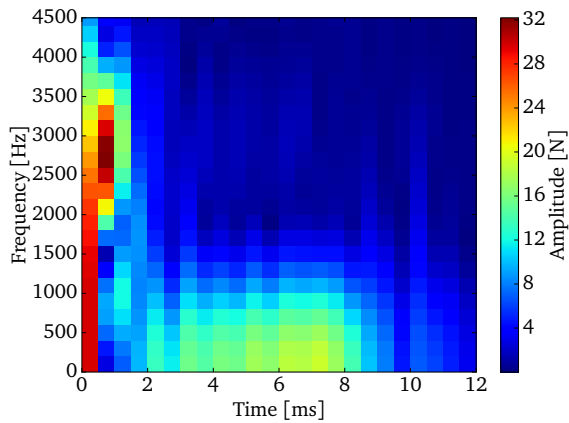
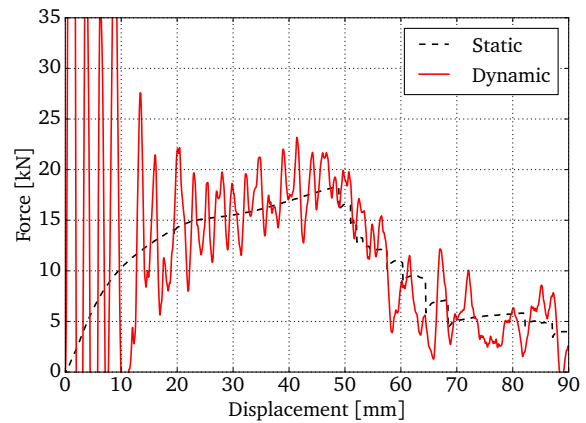**Fig. 9.** Short time Fourier transform of the force signal from test 1.

Fig. 10. Representative force vs. trolley displacement in dynamic test compared to a representative force-displacement curve from the quasi-static tests.

t = 0.0 ms
D = 0.0 mm

t = 4.41 ms
D = 30.0 mm

t = 7.78 ms
D = 48.6 mm

t = 8.88 ms
D = 59.8 mm

t = 12.78 ms
D = 85.4 mm

t = 13.67 ms
D = 91.1 mm
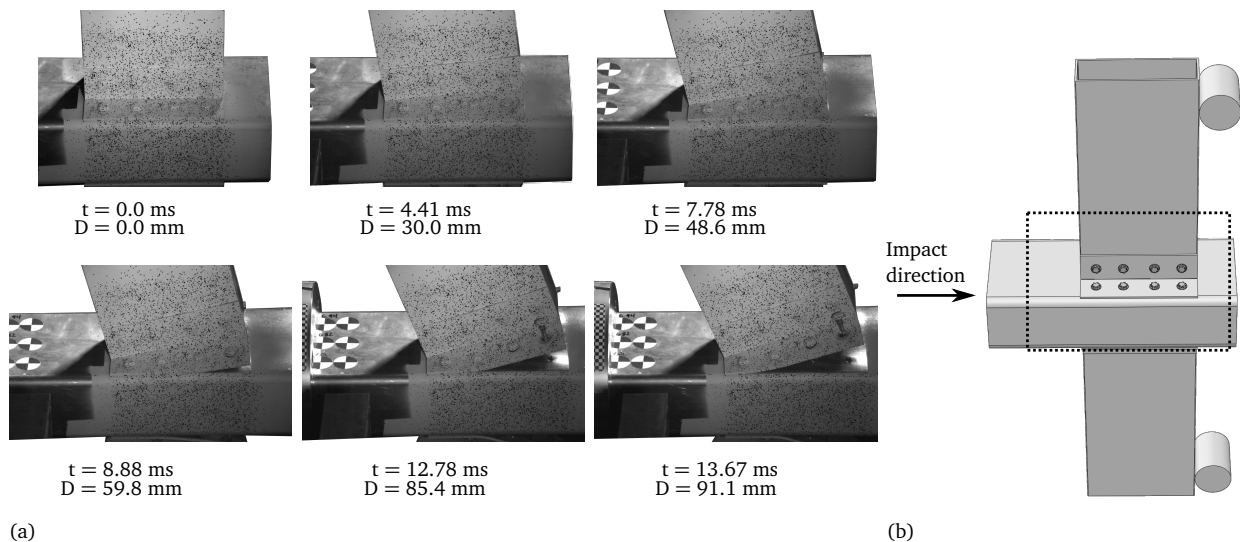
Impact
direction

(a)

(b)

Fig. 11. Pictures of the specimen in dynamic test 1 at various times, as recorded by one of the high-speed cameras. (a) Different frames. (b) Overview showing where the pictures were taken.

206 force-displacement behaviour of the FDS connections between these materials, for this velocity range.

207   Pictures from test 1 taken by one of the high-speed cameras are displayed in Fig. 11a, and an overview
208 highlighting the section depicted is shown in Fig. 11b. The corresponding time and trolley displacement are
209 given for each frame. In the first frame the specimen is undeformed. The second frame was taken at the time
210 corresponding to the displacement where the inner wall of the double-chamber profile buckled in the quasi-static
211 test. Frame three is from just before the force started to drop due to failure of the first connection. In the fourth
212 frame the second connection is about to fail. The fifth was taken shortly before the third connection failed. In the

11

213 last frame the third connection had failed and the test came to an end. The collection of frames clearly shows the
214 propagating failure of the screw connections. Two of the specimens had a symmetric deformation mode, while
215 the remaining three deformed asymmetrically.

3. Finite element modelling

3.1. Numerical set-up

218 In this section the finite element models are explained in detail. All tests (including the single-connector tests)
219 were simulated with the same approach, therefore a general description of the numerical set-up is given here.

3.1.1. Material model

221 The extrusion materials were modelled with a rate-independent hypoelastic-plastic material model. An
222 isotropic yield surface was used, the associated flow rule was assumed, and isotropic work hardening was
223 applied. Since the 6005 and 6060 alloys show slight strain-rate sensitivity (Børvik et al., 2005; Chen et al.,
224 2009) (approximately 10 % increase of flow stress in the strain-rate range from 0.00076 to 1200 s^{-1} for the 6005
225 alloy, somewhat smaller increase for the 6060 alloy), rate sensitivity was not included in the material model.

226 To predict yielding the non-quadratic Hershey yield criterion was used (Hershey, 1954). The aim was to
227 perform large-scale analyses, and a simple (isotropic) yield function was therefore chosen, although the alloys
228 exhibit plastic anisotropy (see Fig. 2 and Table 1). Moreover, it was recently shown by Morin et al. (2017)
229 that the Hershey yield function gave a reasonable description of the global behaviour in large-scale analyses of
230 an aluminium structure exhibiting stronger plastic anisotropy than the alloys in the present work. The yield
231 function is given as

$$f = \phi - (\sigma_0 + R) \leq 0,$$

232 where

$$\phi = \left[\frac{1}{2} \left\{ |s_1 - s_2|^a + |s_2 - s_3|^a + |s_3 - s_1|^a \right\} \right]^{\frac{1}{a}}.$$

233 Here σ_0 is the initial yield stress, R is an isotropic hardening variable, s_1, s_2 and s_3 are the principal deviatoric
234 stresses, and a is a parameter defining the curvature of the yield surface. The value of a was set to 8, as this value
235 has been shown to describe the behaviour of FCC materials (Barlat et al., 2005). To represent work hardening
236 the Voce hardening law was used. With the Voce law, the hardening variable is defined as

$$R = \sum_{i=1}^{N_R} Q_{Ri} \left(1 - \exp\left(-\frac{\theta_{Ri}}{Q_{Ri}} p \right) \right),$$

237 where p is the equivalent plastic strain, N_R is the number of terms, and Q_{Ri} and θ_{Ri} are the saturation value and
238 initial hardening moduli for term i, respectively.

12

239 One quasi-static component test specimen experienced a tear in one angle section. This was considered an
240 anomaly, and it was chosen to not include failure in the material model. Thus, the tear in the angle section cannot
241 be captured with this modelling approach.

242 The material parameters σ_0, Q_{Ri} and θ_{Ri} were found according to the procedure described by Sønstabø et al.
243 (2016). Uniaxial tensile tests were carried out in the extrusion, diagonal and transversal directions, from which
244 the parameters were found by inverse modelling the extrusion direction test using an optimisation algorithm.
245 Typical aluminium values were used for the Young's modulus E, the Poisson ratio ν and the density ρ. The
246 engineering stress strain curves from the simulations are compared to the experiments in Fig. 2. The material
247 parameters are summarised in Table 2.

3.1.2. Macroscopic connection model

249 Due to time step limitations in large-scale simulations, the automotive industry cannot model the FDS
250 connection in detail. Therefore a macroscopic model is required for the connections. Sønstabø et al. (2016)
251 evaluated different state-of-the-art models for FDS connections, and concluded that the self-piercing rivet model
252 presented by Hanssen et al. (2010) was the most accurate and the easiest to calibrate. This model was therefore
253 chosen in this work. Cf. Hanssen et al. (2010) and Sønstabø et al. (2016) for detailed descriptions of the model.
254 A general explanation of the model is given in the following.

255 A node placed between two shell sections' mid-surface defines the location of the connection. Nodes on each
256 shell surface within a user-specified diameter are included in the model. Local normal and tangential forces and
257 a moment are transferred between the sheets, to the nodes within the specified diameter, calculated based on the

Table 2

Material model parameters for the extrusion materials.

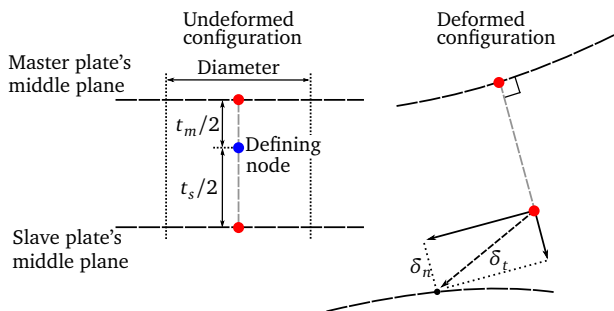| | ρ | E | ν | a | σ_0 | Q_{R1} | θ_{R1} | Q_{R2} | θ_{R2} | Q_{R3} | θ_{R3} |
	[kg/m^3]	[MPa]	[-]	[-]	[MPa]	[MPa]	[MPa]	[MPa]	[MPa]	[MPa]	[MPa]
AA 6060 T6	2700	70000	0.33	8.0	183.2	2.5	5746.3	52.1	985.7	-	-
AA 6005 T6	2700	70000	0.33	8.0	275.7	8.6	7095.1	48.5	702.3	12.2	166.2

Fig. 12. Illustration of macroscopic connection model in plane of maximum opening.

relative motion between the master and slave surfaces. The model is defined in the plane of maximum opening. Figure 12 illustrates the kinematics, where t_m and t_s are the thickness of the master and slave sheet, respectively. The connection follows the master sheet, and the normal and tangential displacements δ_n and δ_t are calculated from the relative displacement to the slave sheet (see Fig. 12). The transferred normal and tangential forces f_n and f_t are calculated as

$$f_n = f_n^{\max} \frac{\delta_n}{\delta_n^{\text{fail}} \eta_{\max}} \hat{f}_n(\eta_{\max})$$

$$f_t = f_t^{\max} \frac{\delta_t}{\delta_t^{\text{fail}} \eta_{\max}} \hat{f}_t(\eta_{\max}),$$

where $f_n^{\max}$ and $f_t^{\max}$ are the maximum forces under pure tension and pure shear loading, respectively, and δ_n^{fail} and δ_t^{fail} are the corresponding local displacements at failure. The empirical functions $\hat{f}_n(\eta_{\max})$ and $\hat{f}_t(\eta_{\max})$ characterise the shape of the force-displacement response. They are defined and illustrated in Fig. 13a. The parameters ξ_n and ξ_t in Fig. 13a are the normalised displacements at which softening starts. Further, $\eta_{\max}$ is a damage parameter defined as the highest value of the effective displacement measure η, i.e. $\eta_{\max} = \max(\eta, \eta_{\max})$. Fig. 13b defines and illustrates the effective displacement measure η, which depends on the mode mixity defined by the angle $\theta = \arctan(\delta_n / \delta_t)$. The variable α makes the mode-mixity dependence damage-dependent, where α_1, α_2 and α_3 are user-parameters.
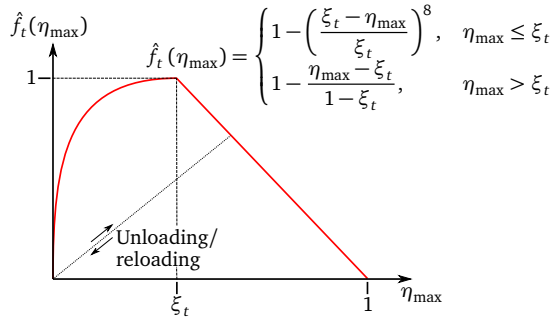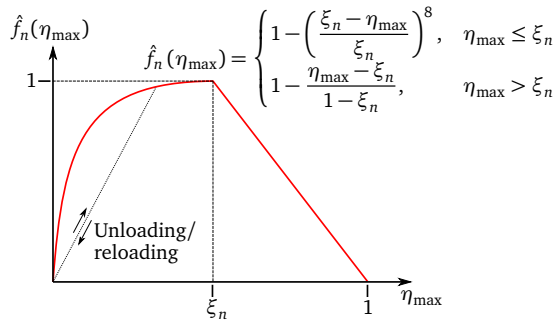
After the forces $f_n^{\max}$ and $f_t^{\max}$ have been determined, the moments transferred to the nodes on the master and slave sheets, M_m and M_s, respectively, are calculated using the relations

$$M_m = \begin{cases} \dfrac{t_m + t_s}{4} f_t & \eta_{\max} < \xi_t \\ \dfrac{t_m + t_s}{4}\left(1 + \dfrac{\eta_{\max} - \xi_t}{1 - \xi_t}\right) f_t & \eta_{\max} \geq \xi_t \end{cases}$$
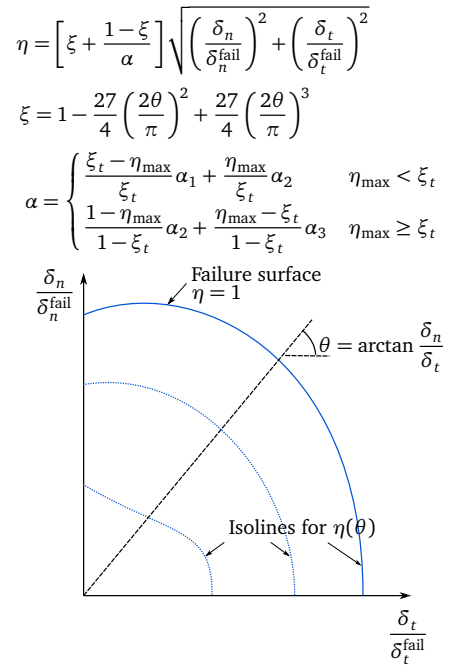
$$M_s = \begin{cases} \dfrac{t_m + t_s}{4} f_t & \eta_{\max} < \xi_t \\ \dfrac{t_m + t_s}{4}\left(1 - \dfrac{\eta_{\max} - \xi_t}{1 - \xi_t}\right) f_t & \eta_{\max} \geq \xi_t \end{cases}.$$

Moment balance is thus satisfied.

The following parameters must be calibrated to tests by the user of the model: $f_n^{\max}$, δ_n^{fail}, ξ_n, $f_t^{\max}$, δ_t^{fail}, ξ_t, α_1, α_2, α_3, and the diameter of influence. They were identified through reverse engineering of the chosen single-connector tests, by comparing global force-displacement curves from simulations to the corresponding curves from experimental tests. Some parameters were taken directly from the experiments ($f_n^{\max}$ and $f_t^{\max}$) or manually tuned to fit the results (δ_n^{fail} and δ_t^{fail}). The remaining parameters were optimised with the Levenberg-Marquardt algorithm, using the mean squared error between the simulation and experimental force-displacement curves as residual function. The optimisation software LS-OPT® (version 5.2) was used. The remaining tension and shear parameters (ξ_n and ξ_t) were optimised first, followed by the mode-mixity parameters (α_1, α_2 and α_3). The diameter of influence affects the stiffness and force response in tension. An increasing diameter increases

14

$$\hat{f}_n(\eta_{\max}) = \begin{cases} 1 - \left(\dfrac{\xi_n - \eta_{\max}}{\xi_n} \right)^8, & \eta_{\max} \leq \xi_n \\ 1 - \dfrac{\eta_{\max} - \xi_n}{1 - \xi_n}, & \eta_{\max} > \xi_n \end{cases}$$

$$\hat{f}_t(\eta_{\max}) = \begin{cases} 1 - \left(\dfrac{\xi_t - \eta_{\max}}{\xi_t} \right)^8, & \eta_{\max} \leq \xi_t \\ 1 - \dfrac{\eta_{\max} - \xi_t}{1 - \xi_t}, & \eta_{\max} > \xi_t \end{cases}$$

$$\eta = \left[\xi + \frac{1 - \xi}{\alpha} \right] \sqrt{ \left(\frac{\delta_n}{\delta_n^{\text{fail}}} \right)^2 + \left(\frac{\delta_t}{\delta_t^{\text{fail}}} \right)^2 }$$

$$\xi = 1 - \frac{27}{4} \left(\frac{2\theta}{\pi} \right)^2 + \frac{27}{4} \left(\frac{2\theta}{\pi} \right)^3$$

$$\alpha = \begin{cases} \dfrac{\xi_t - \eta_{\max}}{\xi_t} \alpha_1 + \dfrac{\eta_{\max}}{\xi_t} \alpha_2 & \eta_{\max} < \xi_t \\ \dfrac{1 - \eta_{\max}}{1 - \xi_t} \alpha_2 + \dfrac{\eta_{\max} - \xi_t}{1 - \xi_t} \alpha_3 & \eta_{\max} \geq \xi_t \end{cases}$$

(a)

(b)

Fig. 13. Definition and illustration of (a) local forces and (b) effective displacement measure in connection model.

²⁸³ the stiffness of the plates. The diameter of the screw head and shaft was 13 and 5 mm, respectively. The average
²⁸⁴ diameter of 9 mm was therefore chosen as diameter of influence of the connection model.

²⁸⁵   No information regarding dynamic single-connector testing of FDS connections is available in the scientific
²⁸⁶ literature. Such tests are difficult to perform. Thus, it is not known if FDS connections are rate sensitive. This
²⁸⁷ model does not exhibit rate sensitivity, including any temperature effects. Based on the small strain-rate sensitivity
²⁸⁸ observed for the present alloys, this seems like a reasonable assumption.

²⁸⁹ *3.1.3. Limitations of macroscopic modelling*

²⁹⁰   There are certain inherent limitations associated with representing the connection with a macroscopic model.
²⁹¹ First of all it is important to understand that the model is merely intended to represent the global force-
²⁹² displacement behaviour of the connection, and not the local deformation. This means that the deformation of the
²⁹³ screw, and the surrounding plate material close to it, is embedded into the macroscopic model. The connection is
²⁹⁴ not physically modelled, it is just represented by a mathematical constraint. This implies that one can not always
²⁹⁵ expect to correctly predict deformation and failure modes occurring in physical tests. For instance, in an FDS
²⁹⁶ connection one side has the screw head on top, while the other has the screw tail sticking out. These geometrical
²⁹⁷ features are not manifested in the model. Sønstabø et al. (2015) and Sønstabø et al. (2016) reported deformation
²⁹⁸ and failure modes occurring due to contact between the tail of the screw and other parts. Such modes can not
²⁹⁹ be captured by this type of model.

³⁰⁰   An example of a limitation is shown in Figs. 14a and 14b which depict the deformation of a peeling test and
³⁰¹ corresponding simulation, respectively. As seen, the deformation pattern was not correctly predicted. In the test
³⁰² a clear bend was visible in the bottom plate close to the screw, while it did not appear in the simulation. The
³⁰³ connection model is symmetric in the sense that the diameter is the same for both sides of the connection. Thus,
³⁰⁴ since the top extrusion had a lower yield stress than the bottom, deformation localised there. In the test, however,
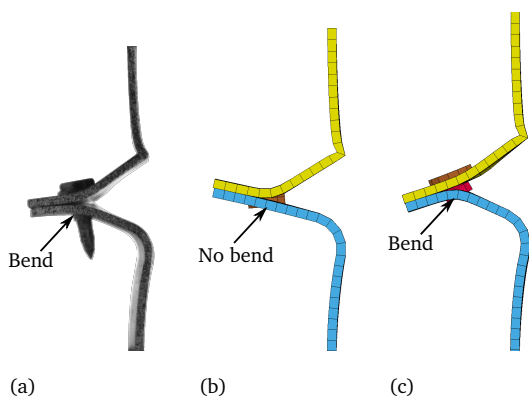

(a)   (b)   (c)

Fig. 14. Deformed peeling specimen (HS-connection) in (a) experiment, (b) simulation with no head and (c) simulation with head.

16

305 the presence of the screw head stiffened the top plate, causing the bottom extrusion to bend as well. As a remedy

306 to try and capture the correct deformation mode it was decided to include a simple model of the screw head,

307 consisting of a circular patch with diameter 13 mm and height 4 mm (see Fig. 1c). The patch was modelled

308 with 20 regular eight-node brick elements with reduced integration, and was attached to the top extrusion's shell

309 mid-surface using a tie constraint. The elements were assigned a purely elastic material model with typical steel

310 parameters ($E = 210000$ MPa, $\nu = 0.33$ and $\rho = 7800$ kg/m^3). Fig. 14c depicts the resulting deformation. As

311 seen the deformation mode now correlated better with the experiments. The solid elements stiffened the top

312 plate as intended, a bend was clearly visible in the bottom plate close to the screw. Therefore it was decided to

313 include the head in all simulations in this study.

314 The final stage in the FDS screw driving process consists of applying a tightening torque to the screw, which

315 causes pre-stressing of the screw and a contact force and friction between the aluminium sections. It should be

316 noted that the macroscopic connection model does not take these effects into account.

3.1.4. Finite element models

318 Fig. 15 depicts the finite element models used in the present investigation. The extrusions were discretised

319 with fully integrated Belytschko-Lin-Tsay shell elements (Belytschko et al., 1984) with a mesh size of 3x3 mm

320 and five integration points through the thickness. This mesh size was chosen because it is known to be used in

321 the automotive industry. The shell thickness was set to 2.43 mm for the rectangular profile, and 2.57 and 1.747

322 mm for the outer and inner wall of the double-chamber profile, respectively. These values were the averages of

323 thickness measurements at various locations. Contact between the different parts was modelled with a surface-to-

324 surface penalty algorithm, where a static friction coefficient of 0.2 was chosen. The connection model described

325 in Section 3.1.2 was applied at all connection locations.

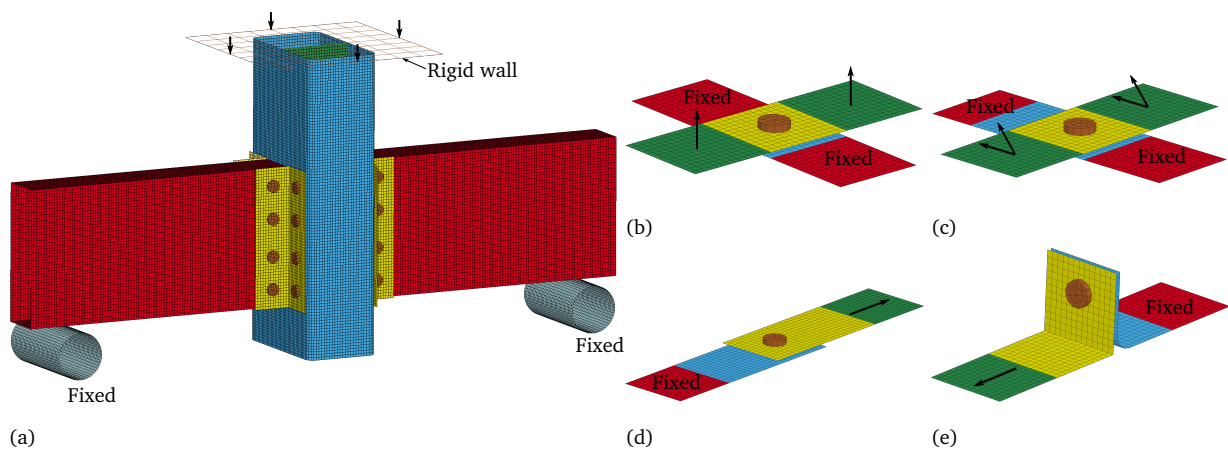326 Since the experimental set-up was the same for the quasi-static and dynamic component tests, the same

Fig. 15. FE models. (a) Component (b) Cross tension. (c) Cross mixed and shear. (d) Single lap-joint. (e) Peeling.

17

numerical set-up was used for the simulations. The model is shown in Fig. 15a. The supports were modelled as rigid bodies, and a friction coefficient of 0.2 was chosen for the contact between the specimen and the supports. The impactor was modelled as a rigid wall. In the quasi-static simulation a prescribed velocity was assigned to the wall (as indicated with arrows in Fig. 15a), and the force was recorded from the reaction force on the wall. In the dynamic simulation the rigid wall was assigned a mass of 400 kg and an initial velocity of 7 m/s. The displacement and acceleration of the rigid wall was recorded, and the force acting on the rigid wall from the specimen was calculated by dividing the wall acceleration by its mass.

The finite element models of the single-connector tests that were used for calibration and validation of the macroscopic connection model are shown in Figs. 15b to 15e. The red and green parts in the figures correspond to the parts of the specimens that were clamped in the experiments. These parts were modelled as rigid bodies. The red parts were constrained against displacement and rotation in any direction, while a prescribed velocity in the loading direction was assigned to the green parts, as shown with arrows. It was thus assumed that no slipping occurred in the clamping system during the single-connector tests. The global force and displacement was recorded from the boundary force and displacement of the green parts, respectively. Details of the single-connector tests are reported in Appendix A.

All simulations were carried out with the explicit solver LS-DYNA® version R9.1 with double precision. For the simulations of the quasi-static tests time scaling was applied to facilitate reasonable computational times. Inertia effects were ensured negligible by confirming that the kinetic energy was insignificant compared to the internal energy of the materials.

3.2. Calibration of connection model parameters

Sønstabø et al. (2016) presented a calibration/validation procedure which was adopted here. The procedure involves calibrating the connection model using simple single-connector tests under controlled loading conditions. A different set of single-connector tests is subsequently used for a first validation of the model. The validation tests should challenge the model under different loadings than the calibration tests and have varying degrees of complexity. A second level of validation is achieved with component tests, which represent more complex loadings on the connections. Sønstabø et al. (2016) calibrated to cross tests in tension, mixed mode and shear. The single lap-joint and peeling tests were used for the first validation step, while a T-component test was used for the second.

In this work the tension parameters $f_n^{\max}$, δ_n^{fail} and ξ_n were calibrated to the cross tension tests, and the mode-mixity parameters α_1, α_2 and α_3 to the cross mixed tests. The shear parameters $f_t^{\max}$, δ_t^{fail} and ξ_t were, however, calibrated to the single lap-joint tests, and not the cross shear tests. The reason for this choice is linked to Fig. 16, which shows the force-displacement response in the cross shear and single lap-joint tests of the HS-connection plotted together. Both the cross shear and single lap-joint tests were shear dominated, and a similar response was expected, and, as seen in the figure, both tests gave the same response until maximum force. After maximum
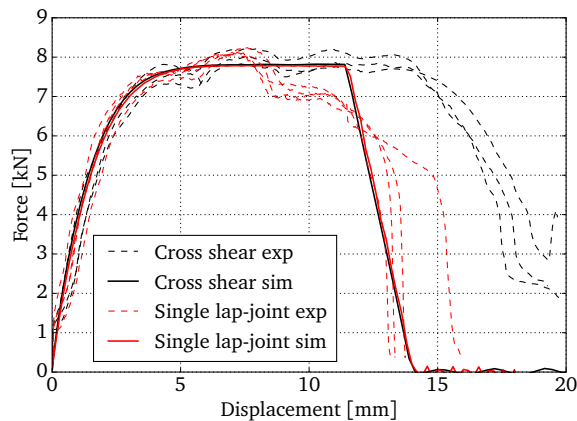
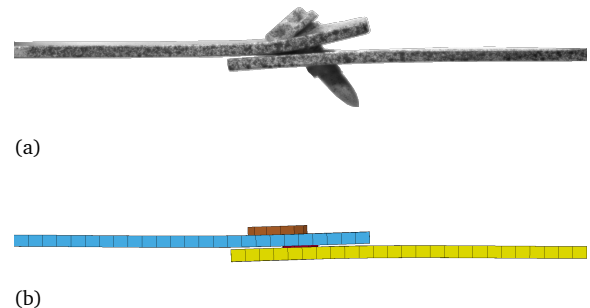**Fig. 16.** Comparison of results from cross shear and single lap-joint tests for the HS-connection.

Fig. 17. Deformed single lap-joint specimen at 10 mm displacement (HS-connection). (a) Experiment. (b) Simulation.

force, however, a significantly dissimilar behaviour developed. In the cross shear tests the force remained at a plateau before a near linear decrease. In the single lap-joint tests the force started to slowly decay immediately after maximum force, before a rapid failure where the force suddenly decreased to zero. This difference is possibly explained by the different boundary conditions in the two tests (readers are referred to Appendix A for details on the test set-ups). During the single lap-joint tests the plates were allowed to bend near the connection (see Fig. 17a). In the cross shear specimens this bending was prevented by more restrictive clamping. Thus, the loading conditions were different in the two tests. The rotation of the screw shaft and the presence of the pre-hole in the top plate facilitated the bending. The macroscopic connection model does not include the screw, however, and hence this effect cannot be captured in the simulations. The simulations of the cross shear and single lap-joint tests gave instead almost identical force-displacement result, see Fig. 16. Fig. 17 compares a picture from the experiments with the deformation in the single lap-joint simulation. It is seen that the simulation did not properly capture the bend of the top plate, with the result that the connection was loaded in almost pure shear. It is believed that if the bending of the plates had been properly captured, a larger tensile component would emerge and effectively reduce the ductility. Therefore a choice had to be made: to try and predict the cross shear or the single lap-joint test. Both approaches were tried, but when the parameters were calibrated to the cross shear test the ductility and maximum force of the peeling test were severely over-predicted. With calibration to the single lap-joint test better predictions in peeling were achieved. For this reason the calibration to the single lap-joint test was chosen. The resulting model parameters are summarised in Table 3.

The force-displacement curves from the simulations of the single-connector tests with all parameters calibrated are compared to the experimental curves in Figs. 18 and 19 for the HH and HS-connections, respectively. As seen, acceptable fits were achieved for the calibration simulations (cross tension, cross mixed and single lap-joint), for both connections. In cross tension the simulation had a higher force response than

19

Table 3

Connection model parameters for the FDS connections.

| | Diameter | f_n^{max} | δ_n^{fail} | ξ_n | f_t^{max} | δ_t^{fail} | ξ_t | α_1 | α_2 | α_3 |
	[mm]	[N]	[mm]	[-]	[N]	[mm]	[-]	[-]	[-]	[-]
HH-connection	9.0	4200	4.2	0.89	7000	13.5	0.60	0.992	0.909	1.299
HS-connection	9.0	5400	6.2	0.82	7800	14.0	0.81	1.176	0.815	1.346

(a)   (b)   (c)
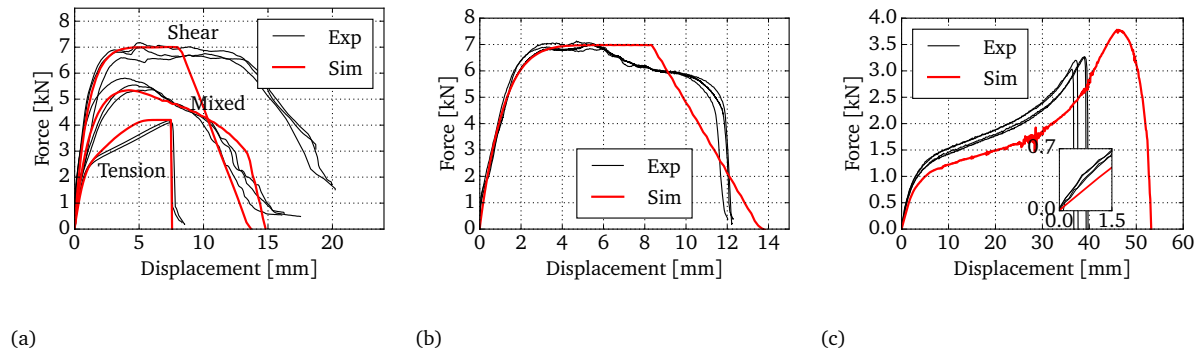
Fig. 18. Simulation results for the single-connector simulations of the HH-connections. (a) Cross simulations. (b) Single lap-joint simulations. (c) Peeling simulations.

(a)   (b)   (c)
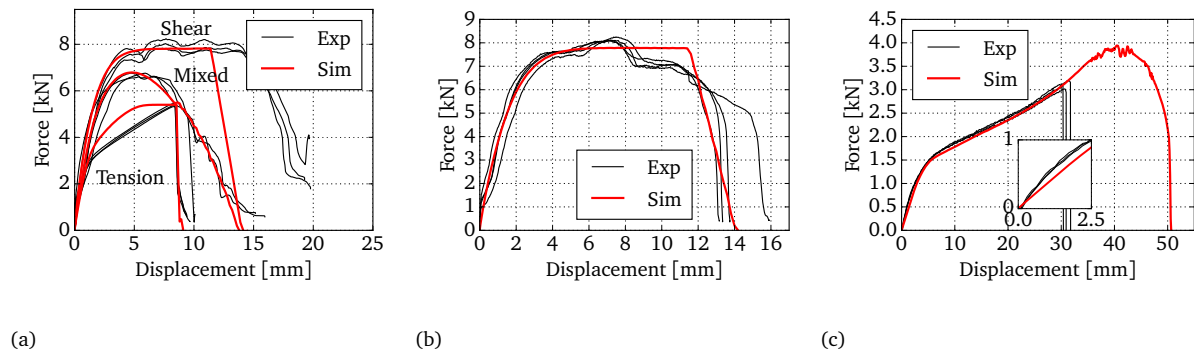
Fig. 19. Simulation results for the single-connector simulations of the HS-connections. (a) Cross simulations. (b) Single lap-joint simulations. (c) Peeling simulations.

in the test, probably caused by the discretisation of the connection. The numerical diameter was set to 9 mm, while the diameter of the screw shaft was 5 mm. Thus, the bottom plate behaved stiffer than in reality, causing a stiffer response in the simulation. The initial stiffness was correctly predicted, however. The two-step failure seen in the single lap-joint tests (slow softening followed by abrupt decrease of force) was not captured, since the connection model features linear softening. The ductility of the cross shear tests was under-estimated (as expected, see discussion above), while the force level was well predicted. In the peeling simulations the ductility and maximum force were over-predicted. Inserted zoomed-in details of the start of the simulations in Figs. 18c and 19c show that the initial stiffness was somewhat under-predicted. These discrepancies between tests and simulations under peeling loading is probably linked to the lack of physics in the connection model, caused by the poor discretisation of the connection, and highlights the challenges associated with macroscopic modelling of connections. Overall, considering the requirements for large-scale crash analyses, the simulations of the single-connector tests gave satisfying results.

4. Component simulations

In this section the component simulation results are presented and discussed. The quasi-static simulation is addressed first, followed by the dynamic. A parametric study from the quasi-static simulation is presented in the end of the section.

4.1. Quasi-static component simulation

The global force-displacement curve from the quasi-static component simulation is presented in Fig. 20a. As seen, an acceptable prediction of the global behaviour was obtained in the simulation. As a first note, the maximum force level was correctly predicted. However, failure initiation occurred approximately 10 mm later than in the test. It is also noted that the value of the force plateau due to buckling of the inner wall was correctly captured, but also occurred approximately 10 mm later than in the test. It is believed that this shift in displacement of approximately 10 mm was caused by under-estimation of the initial stiffness. Fig. 20a includes an inserted box that details the start of the curves, where the under-prediction of the initial stiffness is obvious. A similar observation was made for the peeling test simulations, as shown in Figs. 18c and 19c and discussed in Section 3.2. It is believed that this is an inherent limitation of this type of macroscopic connection model. It seems that the model is incapable of describing the correct elastic deformation. The buckling of the inner wall and the failure initiation occurs when the force reaches a specific level. Thus it seems likely that had the initial stiffness been correctly predicted, the force plateau and maximum force would have occurred for the correct displacements.

Figs. 20b and 20c shows pictures of the deformation seen in the simulation, with numbers indicating the corresponding points on the force-displacement curve. In the pictures showing the inner wall in Fig. 20b one can clearly see how the buckle developed at the force plateau. The pictures close up to the HS-connections in

21

Fig. 20c show how failure propagated along the row of screws. In the experiments the four lowest HS-connections failed one after another, separated with a short time. In the simulation, however, all four failed at the same time. This was probably because the connection model parameters were identical for all connections, while in the experiments the connection failure properties were subjected to natural statistical variation. It is seen that failure in the third screw occurred much later in the simulation than in the experiment. This may indicate that the model is not able to redistribute forces accurately, and that prediction of failure propagation may be difficult with this modelling technique. No failure was observed in the HH-connections, as was the case in the experimental tests.

Fig. 21a shows the evolution of the local connection model forces, f_n and f_t, in the four HS-connections in one of the angle sections. The axial and shear force are plotted together, and the numbers 1-4 signify the connection number from the bottom and up (see Fig. 21b). As expected, in the start the forces were highest in the lowermost connection (number 1). When this connection failed the second connection took over, then the third. It is also seen that the axial force dominated in the three first connections. The shear force component was approximately 50 % lower. This is similar to what is typically observed in simulations of peeling tests, and suggests that the loading on the connections in the component test was somewhat similar to a peeling test.

In addition to the 3 mm mesh size, simulations were run with mesh sizes of 4 and 5 mm. The results are summarised in Fig. 22a. A small mesh-size effect is seen on the force-displacement curve, as failure occurred somewhat later in the simulation with 4 mm mesh size. Embedded in the figure are three pictures of a connection, showing how the mesh size can affect the number of nodes lying within the diameter of influence of the connection
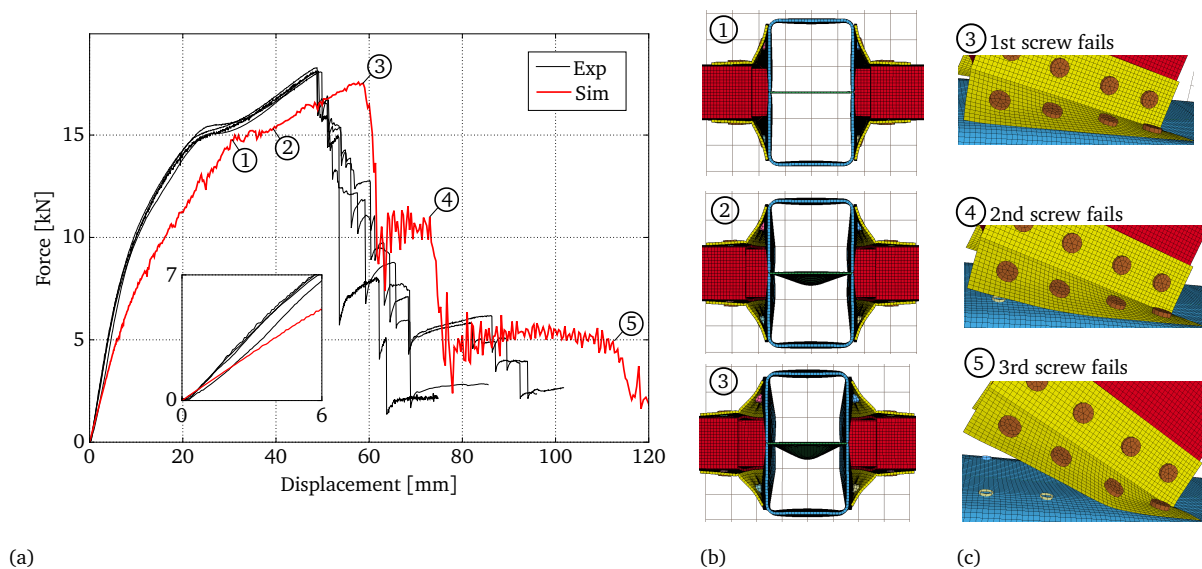

(a) (b) (c)

Fig. 20. Results from quasi-static component simulation. (a) Global force-displacement curve compared with tests. (b) Top view of specimen, showing development of the buckle of the inner wall. (c) Side view showing the propagation of connection failure. Numbers relates each picture to the corresponding point on the force-displacement curve.

22

model. It is apparent that the mesh size can have an effect on the macroscopic response of the connection.

Fig. 22b shows the effect of varying the friction coefficient between the specimen and supports from 0.0 to 0.5. As is typical for three-point bending tests, an effect is seen on the force level as well as the initial stiffness. Fig. 22c shows that the effect of varying the friction coefficient between the different parts in the component is insignificant. For friction coefficients 0.0 and 0.1 the force plateau at 15 kN disappeared, which was due to a change in deformation mode. Instead of buckling of the inner wall, the corner of the rectangular profiles collapsed. Considering that this did not occur in the tests, this mode was judged to be non-physical.

Fig. 23 shows the effect of excluding the elastic solid elements resembling the screw head. The simulation without the head was run with connection model parameters that were specifically calibrated without the head (i.e. not the ones reported in Table 3). As seen, without the head the accuracy of the results was significantly decreased. The maximum force and failure displacements became significantly over-predicted. This supports the choice of including the simple model of the screw head when modelling FDS connections with this model.

4.2. Dynamic component simulation

Fig. 24 presents the force-displacement curve from the dynamic component simulation compared with experiments. Only one experimental curve is included for clarity. The quasi-static simulation result is also plotted. The dynamic simulation curve starts with several large peaks, separated by gaps with zero force. This was due to multiple impacts between the rigid wall and the specimen, each peak corresponding to one hit. The force was zero between the peaks because the rigid wall then had zero acceleration. The phenomenon with several hits was also seen in the experiments (see Fig. 7), but lasted for a significantly shorter period of time. The difference in "time
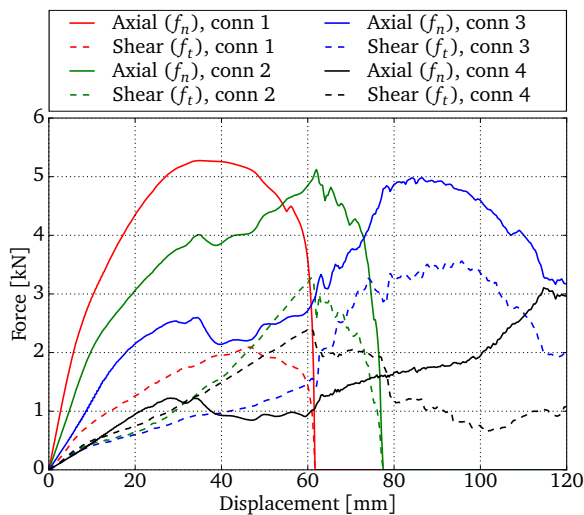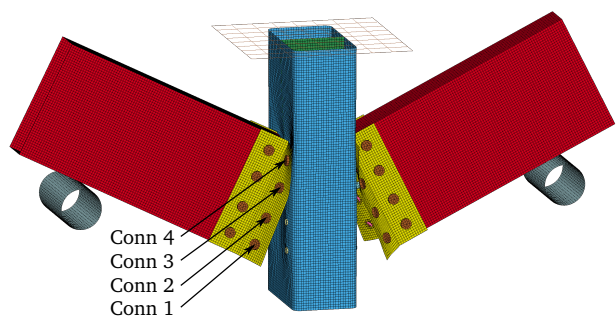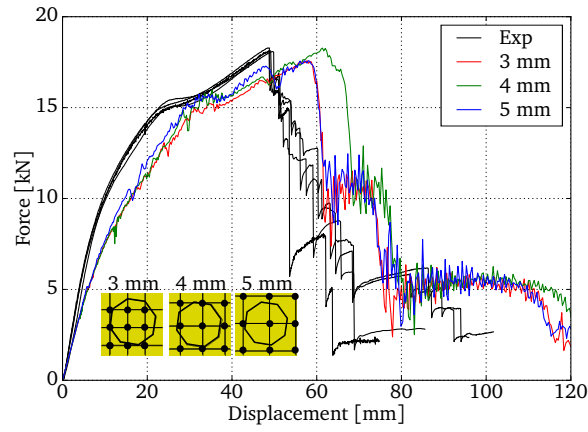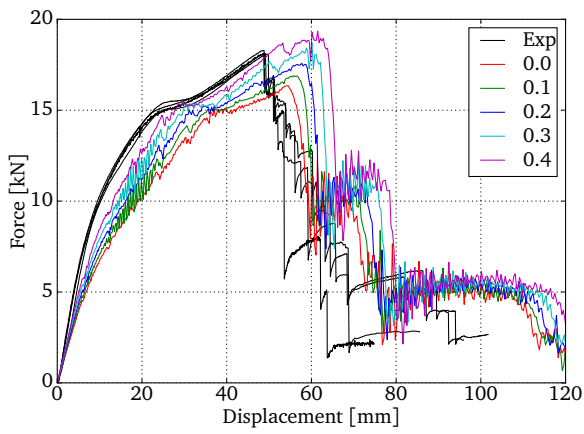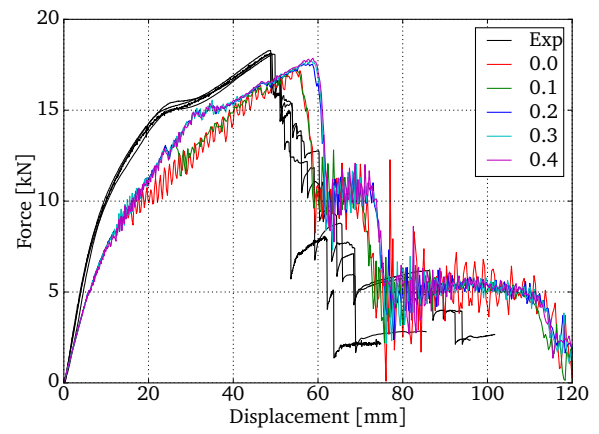

(a)   (b)

Fig. 21. Local forces in connection model along one row of HS-connections. (a) Forces. (b) Illustration of connections 1 to 4.

23

(a)

(b)

(c)

Fig. 22. Effect of varying the (a) mesh size, (b) friction coefficient between the supports and the specimen, and (c) the friction coefficient in the specimen.
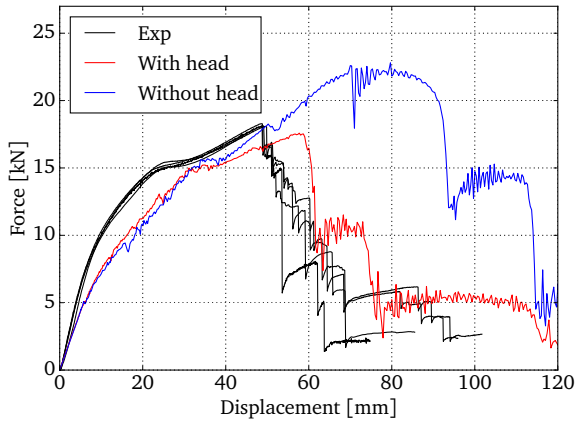
Fig. 23. Quasi-static component simulation with and without screw head.

without contact" between simulation and experiment was possibly a consequence of the under-estimated initial stiffness. Had the initial stiffness been correctly predicted, it is believed that the time with no contact between the load cell and the specimen would have been better estimated. After 30 mm displacement, firm contact was achieved between the specimen and the rigid wall, and from here on the force level correlated adequately with the experiments.

The curves from the dynamic and quasi-static simulations more or less overlaid each other after 30 mm displacement, except that the dynamic curve oscillated. This supports the observation that inertia effects in the specimen did not alter the structural response of the component. Differences between simulations and tests were present both in the quasi-static and dynamic cases, and were thus not related to dynamic effects. Therefore it was sufficient to address the quasi-static case to evaluate differences between tests and simulation.

4.3. Parametric study in quasi-static component simulation

As discussed in Section 2.3, variations in the structural response of FDS connections can occur due to geometrical and process variations. To study how such variations can affect the test results, simulations were carried out with connection model parameters δ_n^{fail}, δ_t^{fail}, f_n^{max} and f_t^{max} randomly distributed using a regular Gauss distribution. The mean value μ was set to the initial parameter value, and the standard deviation σ was chosen based on the scatter seen in the single-connector tests (Fig. A.2). The chosen values are given in Table 4. Each of the HS-connections were assigned a parameter value picked randomly from the Gauss distribution. Only one parameter (δ_n^{fail}, δ_t^{fail}, f_n^{max} or f_t^{max}) was changed per simulation, thus in total four simulations were carried out. The resulting force-displacement curves are plotted in Fig. 25a, with zoomed-in details in Fig. 25b. As seen, an effect was seen only for the parameter δ_n^{fail}, where the deformation mode changed from symmetrical to unsymmetrical (see Figs. 25c and 25d). This makes sense, since the loading on the connections was tensile
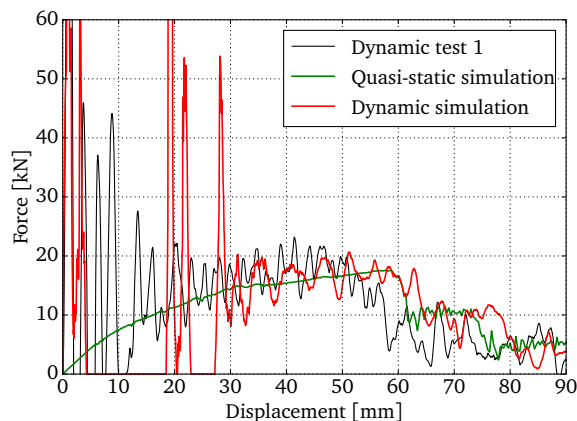
25

Fig. 24. Force-displacement curve from simulation of dynamic component test.

Table 4

Parameters used in statistical distributions of connection model parameters.

Parameter	μ	σ
δ_n^{fail} [mm]	6.2	0.087
δ_t^{fail} [mm]	14.0	0.94
$f_n^{\max}$ [N]	5400	53.0
$f_t^{\max}$ [N]	7800	60.7

dominated (recall Fig. 21), and since the test was displacement controlled. When one side had lower ductility, an unsymmetrical deformation mode was expected. This supports the discussion in Section 2.3.

5. Summary and conclusions

In this work a novel component test suited for quasi-static and dynamic testing of flow-drill screw connections was presented. The component consisted of two rectangular extrusions of aluminium alloy AA 6060 in T6 temper joined to a double-chamber profile of aluminium alloy AA 6005 in T6 temper. The quasi-static tests were conducted in a regular tensile testing machine, while the dynamic were performed in a pendulum accelerator rig designed for impact testing. The tests were simulated with large-scale finite element models, where a macroscopic model for large-scale simulations was used for the connections. An improvement of the connection modelling technique was presented.

The following main conclusions were drawn from the experimental part of the study:

– High test repeatability was obtained in the component tests, which makes the presented component suitable for validation of numerical models.
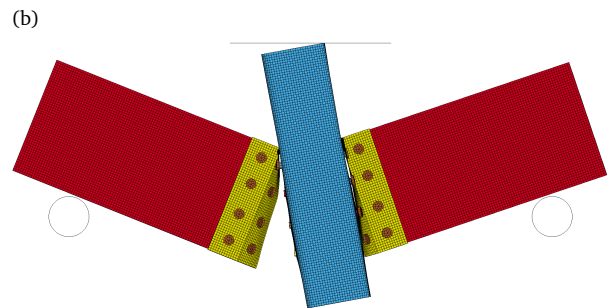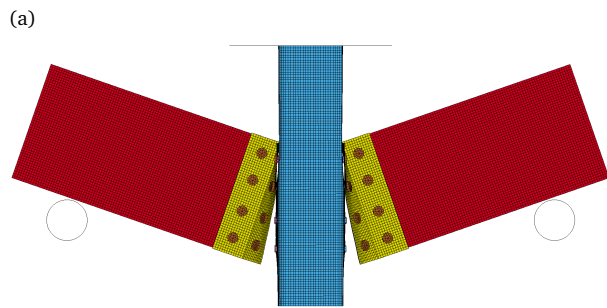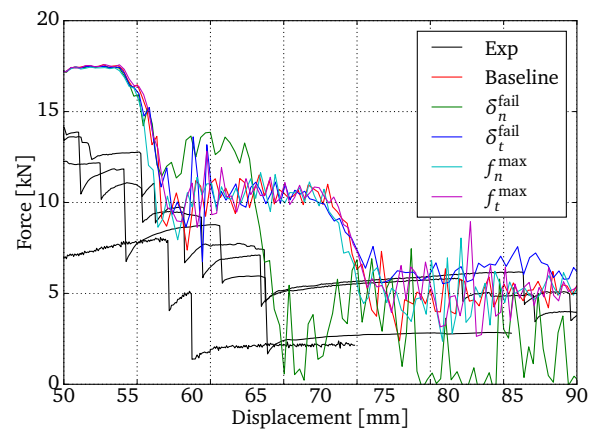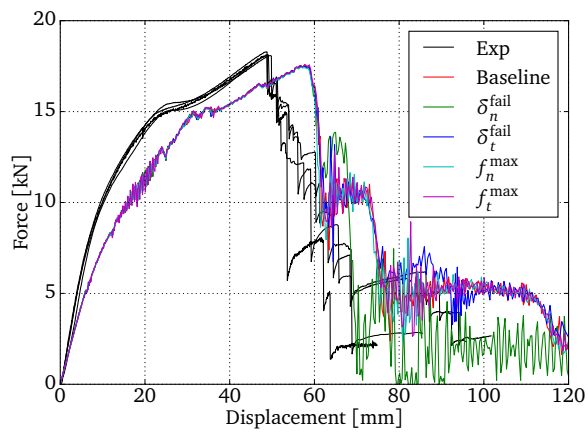
26

Fig. 25. Effect of statistical variation of connection model parameters. (a) Force curves. (b) Zoomed-in force curves. (c) Symmetrical component deformation. (d) Unsymmetrical deformation when varying δ_n^{fail}.

- The force-displacement curves from the dynamic and quasi-static tests were similar, indicating that no global inertia and strain-rate effects in the specimen influenced the structural response, for the investigated velocity range.

- In both the quasi-static and dynamic component tests a propagating connection failure was achieved. The test is thus suited to evaluate failure propagation in numerical simulations.

The following main conclusions were drawn from the numerical part of the study:

- By including a simple elastic model of the screw head, the component simulation results were significantly improved. It is advised to include a model of the head when modelling flow-drill screw connections.

- Good agreement with experiments was obtained for the quasi-static component simulation. The initial stiffness was too low, causing buckling of the inner wall, maximum force and failure initiation to occur somewhat later than in the test. The low initial stiffness indicates that the current macroscopic model is incapable of representing the correct elastic deformations.

- Since each HS-connection had identical connection model parameters, failure initiated simultaneously in the lowest connection on all sides of the component. In the experiment they did not fail at the same time, because of natural variation of the mechanical properties of the connections. Nevertheless, good correlation was seen for the failure of the two first connections, which occurred somewhat later than in the experiments. The third connection was predicted to fail much later than in the experiments, indicating that prediction of failure propagation may be difficult with this modelling technique.

- The force-displacement curve from the dynamic simulation correlated adequately with the experiments. The time without contact between the trolley and the specimen was significantly large, and failure initiation occurred somewhat later than the experiments. However, the force-displacement curves from the quasi-static and dynamic simulations agreed well, indicating that the above observations were caused by the low initial stiffness. This further indicated that the physics of the dynamic test were well captured in the simulation.

Appendix A   Characterization of connections

518   The FDS connections in the joint were characterised by means of single-connector tests. Specimens with plates

519   of varying geometry joined by a single screw were pulled apart in different directions, producing various loadings

520   on the connections. The main reason for performing such tests was that they were necessary to calibrate and

521   validate the macroscopic connection model for the large-scale finite element simulation of the component test.

522   In addition, they provided useful knowledge of the structural performance of the connections under different

523   loadings, for instance maximum force, stiffness and ductility, as well as information about failure mechanisms.

524   The single-connector tests carried out in this work were cross tests in tension, mixed mode and shear, and

525   single lap-joint and peeling tests. The test set-ups and results are presented in the following sections.

526   *A.1   Cross tests*

527   Fig. A.1a illustrates the principle of the cross tests. The coloured areas in the figure were clamped in the tests.

528   To allow for relative sliding of the plates, only half of the area on one side of the bottom plate was clamped in

529   the cross mixed and shear tests. This is indicated with a lighter red colour where the clamping was omitted. The

530   bottom plate was fixed, while the top plate was pulled in the direction of the arrows in the figure.

531   A schematic drawing of the cross test specimen is shown in Fig. A.1b, where the clamped areas are indicated

532   with grey colour. The darker grey indicates the area where a smaller clamping was used in the cross mixed and

533   shear tests.

534   Fig. A.1c shows a principle drawing of the cross tension test set-up. The specimen was mounted on two steel

535   fixtures, using screws and clamping blocks. A picture of the set-up is shown in Fig. A.1d. The steel fixtures were

536   placed in a regular Instron tensile testing machine, where they were pulled apart in the vertical direction. Pure

537   tensile loading was ensured by hinging the fixture in each end. The pulling force was measured with a load cell

538   mounted in series between the top fixture and the cross beam of the testing machine. A camera was used to take

539   photographs during the tests, which were later used to measure the relative displacement of the steel fixtures

540   with a DIC method.

541   The shear and mixed mode cross tests were carried out using a rig designed for testing of connections under

542   controlled boundary conditions. Principle drawings of the set-up are shown in Figs. A.1e and A.1f, and Fig. A.1g

543   shows a picture of the mixed-mode set-up. The cross specimen was clamped to two main steel parts (denoted part

544   1 and part 2 in Fig. A.1) with screws and clamping blocks. The main steel parts were placed inside a cylindrical

545   steel casing, to prevent rotation and translation of part 1 in other directions than in the pulling direction, thus

546   ensuring controlled boundary conditions in the test. Part 1 was attached to the cylinder with a roller system,

547   allowing for smooth motion in the loading direction, whereas part 2 was bolted to the casing. The rig was

548   designed such that the load application line passed exactly through the centre of the specimen (as indicated with

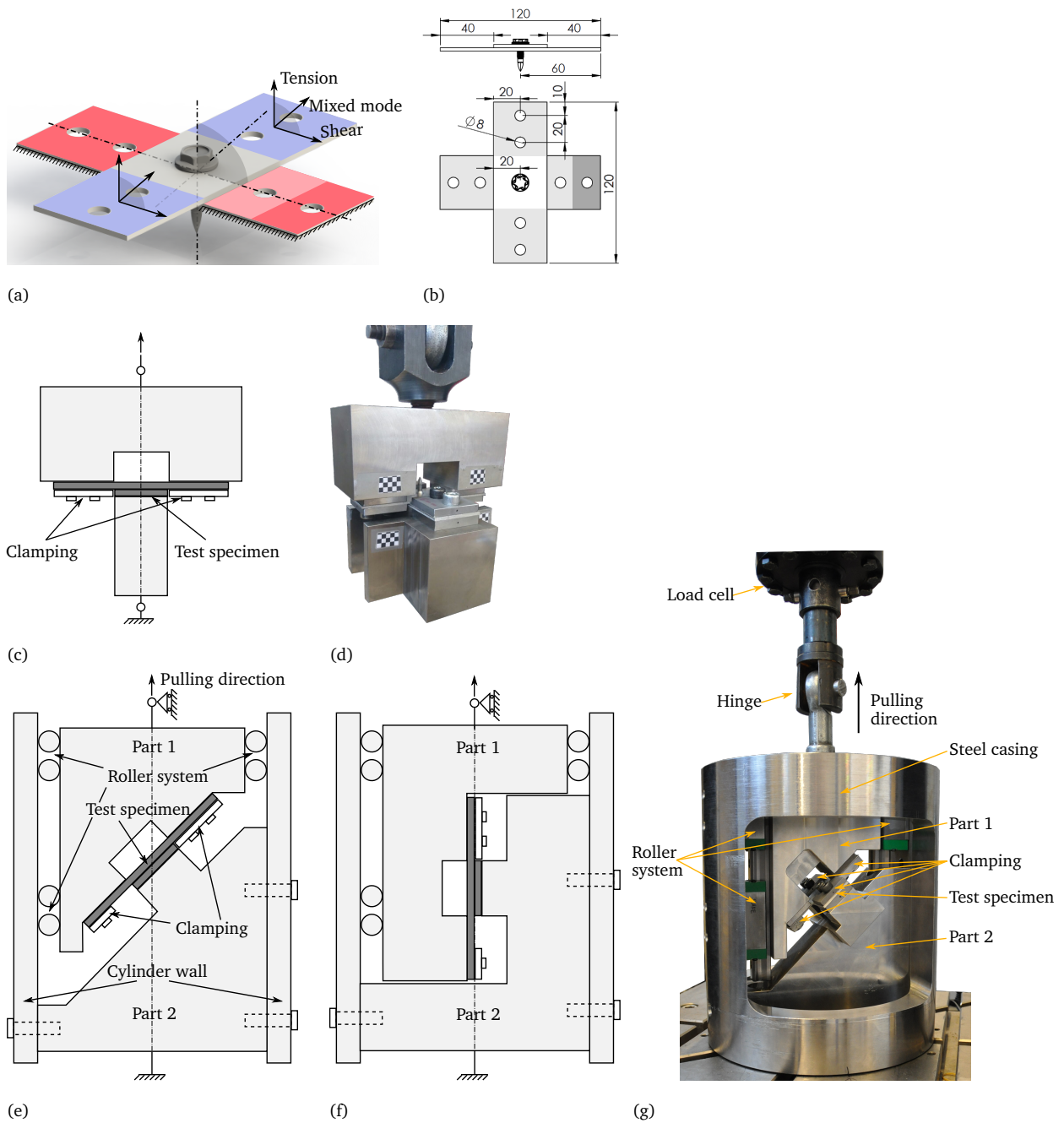549   stippled-dotted lines in Figs. A.1a, A.1c, A.1e and A.1f).

Fig. A.1. Illustrations of the set-ups in the cross tests. (a) Principle of the cross tests. (b) Drawing of the cross test specimen. (c) Principle drawing of the tension set-up. (d) Picture of the tension set-up. (e) Principle drawing of the mixed-mode set-up. (f) Principle drawing of the shear set-up. (g) Picture of the mixed mode set-up.

The rig was placed in a regular Instron tensile testing machine. The rig was hinged in the top, and attached to the testing machine with a single bolt between the centre of the bottom of part 2 and the testing machine. A load cell was mounted between the top hinge and the cross-beam of the testing machine. It was confirmed by in-house testing that the friction force in the rollers was negligible compared to the pulling force, and thus that the force measured was equal to the force transmitted through the specimen. The clamping of the specimen was carefully monitored to verify that no slipping occurred. A camera was used to take photographs during the tests, to later measure the rigid-body motion of parts 1 and 2 with DIC. It was verified that the rotation and translation in other directions than the pulling direction were negligible. The cross-head velocity in all cross tests was set to 5 mm/min, which was assumed to render quasi-static conditions.

Results from cross tests of both connections are presented as force-displacement curves in Fig. A.2, where the displacement was calculated as the relative displacement between the top and bottom steel parts using DIC. The two connections behaved similarly in terms of force-displacement curves and deformation modes. Both connections were strongest in shear and weakest in tension. Due to the significantly stronger bottom extrusion, the HS-connection sustained higher forces than the HH-connection. Mechanical tests on connections are expected to show some degree of scatter in the results, due to uncertainties in the joining process (e.g. rotational speed, tightening torque, cleanliness). The repeatability obtained here was considered acceptable.

In tension the majority of the measured displacement was caused by plastic bending of the plates. Little deformation occurred locally in the connection before the maximum force capacity was reached, where the threads in the bottom extrusion were abruptly stripped. The maximum force in tension was approximately 30 % higher for the HS-connection, and the displacement at failure was approximately 13 % higher.
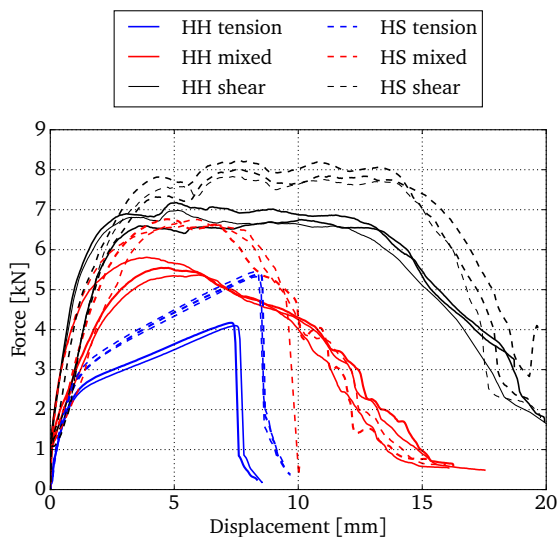

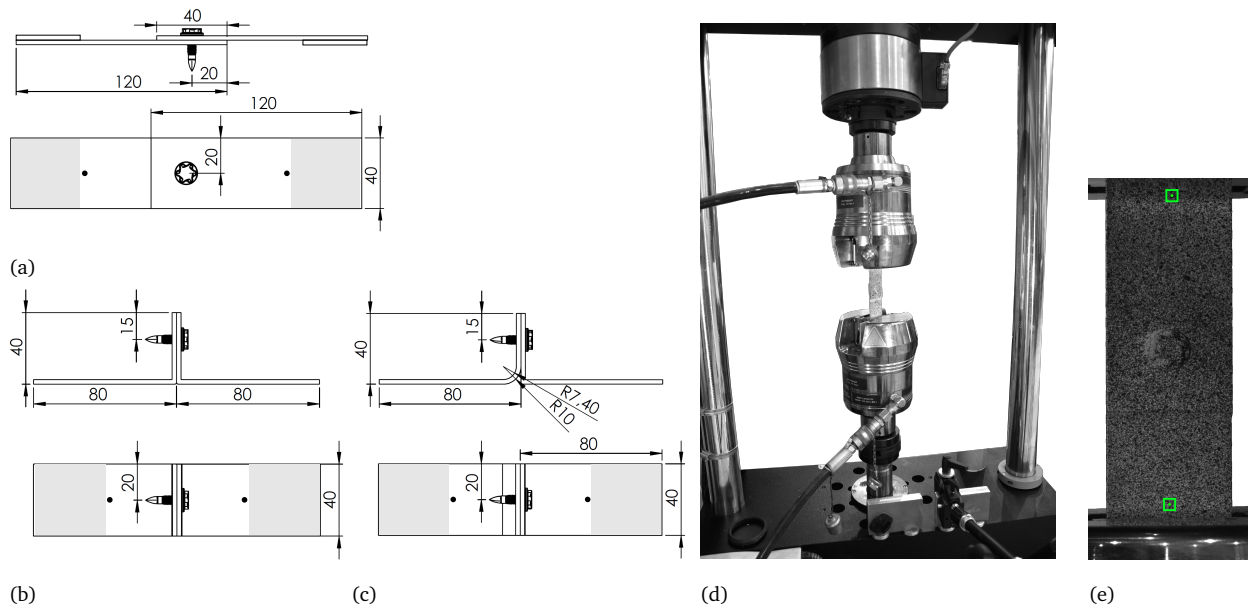**Fig. A.2.** Force-displacement curves from cross tests.

Fig. A.3. Illustrations of the single lap-joint and peeling test set-ups. (a) Schematic drawing of the single lap-joint specimen. (b-c) Schematic drawings of the peeling specimens. Grey areas indicate the gripping area of the clamps. Black dots indicate the locations from where local relative displacement was recorded. (d) Picture of test set-up. (e) Example of pictures used to measure local relative displacement (tracking points shown with green boxes).

In mixed mode the force increased gradually until maximum force was reached. For the HH-connection the force started to decrease instantly after maximum force was achieved, while for the HS-connection the force flattened out to a small plateau before decreasing. The screw rotated slightly during testing, such that threads were engaged on one side of the screw hole only. The specimens failed by thread stripping from the bottom plate. The maximum force was approximately 15-20 % higher for the HS-connection. The ductility was similar.

A significant force plateau was observed for both connections in shear, after which the force dropped nearly linearly. The maximum force was approximately 15 % higher for the HS-connection, and the ductility was similar. In these tests the screw rotated significantly, engaging threads on only one side of the screw hole, and the connections failed by a through-thickness shear failure.

A.2   Single lap-joint and peeling tests

Drawings of the single lap-joint and peeling specimens are shown in Figs. A.3a to A.3c. In the single lap-joint test the only difference for the two connections was the thickness of the bottom extrusion, otherwise the specimen geometry was unchanged. The geometry of the peeling specimen, on the other hand, was different for the two connections, hence is the drawing for each of them included.

The single lap-joint and peeling specimens were clamped with hydraulic grips in a regular Instron tensile test machine (clamping area is indicated with grey colour in Figs. A.3a to A.3c). Since the clamps were aligned in the

testing machine, it was chosen to glue additional plates on the clamping area of the single lap-joint tests, to avoid deformation of the specimen upon clamping. The extra plates are indicated in Fig. A.3a. The specimens were pulled apart under displacement control at a cross-head velocity of 2.5 and 5 mm/min for the single lap-joint and peeling tests, respectively. The pulling force was recorded by a load cell mounted between the upper clamp and the cross-head beam of the testing machine. The local relative displacement was recorded by tracking two points on the specimen (indicated with black dots in Figs. A.3a to A.3c) with a camera taking one picture per second during testing. Fig. A.3d depicts the test set-up and Fig. A.3e shows an example of a picture during a single lap-joint test, where the tracking points for local relative displacement are indicated with green boxes.

Resulting force-displacement curves are shown in Fig. A.4. In the single lap-joint test the HS-connection gave approximately 17 % higher force and approximately 13 % higher ductility than the HH-connection. After maximum force was reached, the force decreased slowly until a rapid failure occurred where it dropped to zero. The screw and top plate rotated during deformation, and the connection failed by thread stripping from the bottom plate.

In the peeling test highest force was achieved for the HS-connection. The maximum force, however, was similar for the two connections. The specimen with the HH-connection was approximately 24 % more ductile than with the HS-connection. These observations are explained by the stronger bottom extrusion in the HS-connection.

References

Barlat, F., Aretz, H., Yoon, J., Karabin, M., Brem, J., Dick, R., 2005. Linear transfomation-based anisotropic yield functions. International Journal of Plasticity 21 (5), 1009 – 1039. https://doi.org/10.1016/j.ijplas.2004.06.004

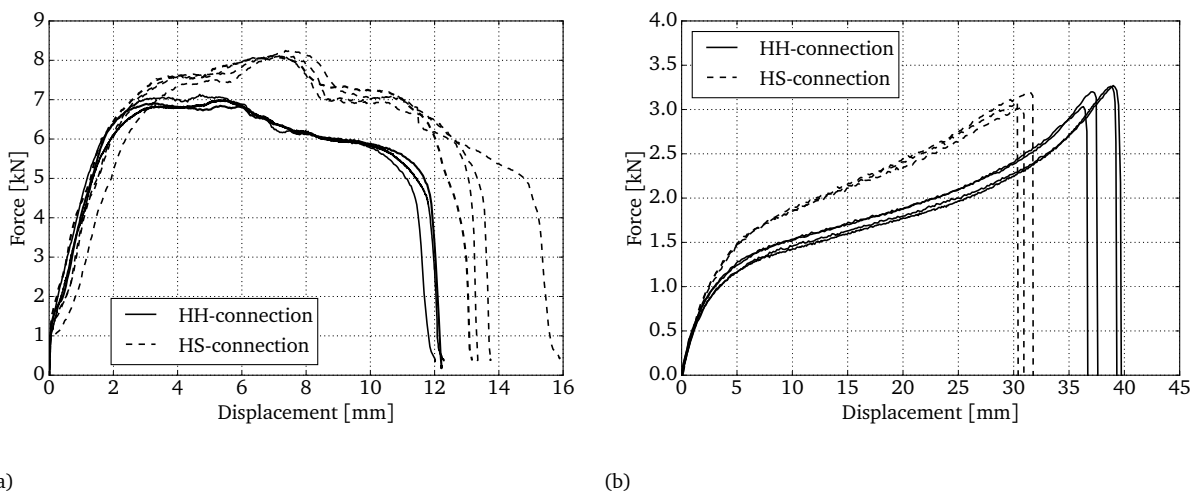(a)   (b)

Fig. A.4. Force-displacement curves from (a) single lap-joint and (b) peeling tests.

33

Belingardi, G., Goglio, L., Rossetto, M., 2005. Impact behaviour of bonded built-up beams: experimental results. International Journal of Adhesion and Adhesives 25 (2), 173 – 180. https://doi.org/10.1016/j.ijadhadh.2004.06.004

Belytschko, T., Lin, J. I., Chen-Shyh, T., 1984. Explicit algorithms for the nonlinear dynamics of shells. Computer Methods in Applied Mechanics and Engineering 42 (2), 225 – 251. https://doi.org/10.1016/0045-7825(84)90026-4

Børvik, T., Clausen, A. H., Eriksson, M., Berstad, T., Hopperstad, O. S., Langseth, M., 2005. Experimental and numerical study on the perforation of AA6005-T6 panels. International Journal of Impact Engineering 32 (1), 35 – 64, fifth International Symposium on Impact Engineering. https://doi.org/10.1016/j.ijimpeng.2005.05.001

Carlberger, T., Stigh, U., 2010. Dynamic testing and simulation of hybrid joined bi-material beam. Thin-Walled Structures 48 (8), 609 – 619. https://doi.org/10.1016/j.tws.2010.03.003

Chen, W., 2001. Experimental and numerical study on bending collapse of aluminum foam-filled hat profiles. International Journal of Solids and Structures 38 (44), 7919 – 7944. https://doi.org/10.1016/S0020-7683(01)00094-4

Chen, Y., Clausen, A., Hopperstad, O., Langseth, M., 2009. Stress-strain behaviour of aluminium alloys at a wide range of strain rates. International Journal of Solids and Structures 46 (21), 3825 – 3835. https://doi.org/10.1016/j.ijsolstr.2009.07.013

Fagerholt, E., 2012. Field measurements in mechanical testing using close-range photogrammetry and digital image analysis. Ph.D. thesis, Norges teknisk-naturvitenskapelige universitet (NTNU).

Grimsmo, E., Clausen, A., Langseth, M., Aalberg, A., 2015. An experimental study of static and dynamic behaviour of bolted end-plate joints of steel. International Journal of Impact Engineering 85, 132 – 145. https://doi.org/10.1016/j.ijimpeng.2015.07.001

Hanssen, A., Olovsson, L., Porcaro, R., Langseth, M., 2010. A large-scale finite element point-connector model for self-piercing rivet connections. European Journal of Mechanics - A/Solids 29 (4), 484 – 495. https://doi.org/10.1016/j.euromechsol.2010.02.010

Hanssen, A. G., Auestad, T., Tryland, T., Langseth, M., Jan 2003. The kicking machine: A device for impact testing of structural components. International Journal of Crashworthiness 8 (4), 385–392. https://doi.org/10.1533/ijcr.2003.0246

Hershey, A., 1954. The plasticity of an isotropic aggregate of anisotropic face-centered cubic crystals. Journal of Applied Mechanics-Transactions of the Asme 21 (3), 241–249.

Hoang, N.-H., Hanssen, A.-G., Langseth, M., Porcaro, R., 2012. Structural behaviour of aluminium self-piercing riveted joints: An experimental and numerical investigation. International Journal of Solids and Structures 49 (23), 3211 – 3223. https://doi.org/10.1016/j.ijsolstr.2012.05.039

Morin, D., Kaarstad, B., Skjaa, B., Hopperstad, O., Langseth, M., 2017. Testing and modelling of stiffened aluminium panels subjected to quasi-static and low-velocity impact loading. International Journal of Impact Engineering 110 (Supplement C), 97 – 111, special Issue in honor of Seventy Fifth Birthday of Professor N. K. Gupta. https://doi.org/10.1016/j.ijimpeng.2017.03.002

Porcaro, R., Hanssen, A., Aalberg, A., Langseth, M., 2004. Joining of aluminium using self-piercing riveting: testing, modelling and analysis. International journal of crashworthiness 9 (2), 141–154. https://doi.org/10.1533/ijcr.2004.0279

Qi, C., Sun, Y., Hu, H.-T., Wang, D.-Z., Cao, G.-J., Yang, S., 2016. On design of hybrid material double-hat thin-walled beams under lateral impact. International Journal of Mechanical Sciences 118 (Supplement C), 21 – 35. https://doi.org/10.1016/j.ijmecsci.2016.09.009

Skovron, J., Mears, L., Ulutan, D., Detwiler, D., Paolini, D., Baeumler, B., Claus, L., 09 2014. Characterization of flow drill screwdriving process parameters on joint quality. SAE Int. J. Mater. Manf. 8, 35–44. https://doi.org/10.4271/2014-01-2241

Skovron, J. D., Prasad, R. R., Ulutan, D., Mears, L., Detwiler, D., Paolini, D., Baeumler, B., Claus, L., 2015. Effect of Thermal Assistance on the Joint Quality of Al6063-T5A During Flow Drill Screwdriving. Journal of Manufacturing Science and Engineering 137 (5), 051019. https://doi.org/10.1115/1.4031242

Sønstabø, J. K., Holmstrøm, P. H., Morin, D., Langseth, M., 2015. Macroscopic strength and failure properties of flow-drill screw connections. Journal of Materials Processing Technology 222, 1 – 12. https://doi.org/10.1016/j.jmatprotec.2015.02.031

Sønstabø, J. K., Morin, D., Langseth, M., 2016. Macroscopic modelling of flow-drill screw connections in thin-walled aluminium structures. Thin-Walled Structures 105, 185 – 206. https://doi.org/10.1016/j.tws.2016.04.013

Szlosarek, R., Karall, T., Enzinger, N., Hahne, C., Meyer, N., 2013. Mechanical testing of flow drill screw joints between fibre-reinforced

649   plastics and metals. Materials Testing 55 (10), 737–742. https://doi.org/10.3139/120.110495

650   Xiang, Y., Wang, Q., Fan, Z., Fang, H., 2006. Optimal crashworthiness design of a spot-welded thin-walled hat section. Finite Elements in

651   Analysis and Design 42 (10), 846 – 855. https://doi.org/10.1016/j.finel.2006.01.001

652   Zhou, Y., Lan, F., Chen, J., 2011. Crashworthiness research on s-shaped front rails made of steel–aluminum hybrid materials. Thin-Walled

653   Structures 49 (2), 291 – 297. https://doi.org/10.1016/j.tws.2010.10.007